Grant Agreement No: 101094300

MuCoL

A Design Study for a Muon Collider complex at 10 TeV centre of mass

Horizon Europe Framework Programme

MILESTONE REPORT

PRELIMINARY PARAMETERS

MILESTONE NO 5

Document identifier:	MuCol_Mil_5_WP1_v1-0.pdf
DOI:	10.5281/zenodo.13970100
Due date of milestone:	31/10/2024 (End of Month 20)
Justification for delay:	New deadline approved by EU Project Officer
Work package:	WP1 – Coordination and Communication
Lead beneficiary:	CERN
Report release date:	28/10/2024
Document version:	1.0
Document status:	Final

Abstract:

This document is comprised of a collection of updated preliminary parameters for the key parts of the muon collider. The updated preliminary parameters follow on from the October 2023 Tentative Parameters Report. Particular attention has been given to regions of the facility that are believed to hold greater technical uncertainty in their design and that have a strong impact on the cost and power consumption of the facility. The data is collected from a collaborative spreadsheet and transferred to overleaf.

For more information on MuCol, its partners and contributors please see https://mucol.web.cern.ch/

Funded by the European Union (EU). Views and opinions expressed are however those of the author(s) only and do not necessarily reflect those of the EU or European Research Executive Agency (REA). Neither the EU nor the REA can be held responsible for them.

Delivery Slip

	Name	Partner	Date
Authored by	IMCC & MuCol Authors	All	01/10/2024
Edited by	R. Taylor	CERN	11/10/2024
Reviewed by	D. Schulte [Project Leader] C. Rogers [Deputy Project Leader] M. Lancellotti [Administrative coordinator]	CERN UKRI CERN	25/10/2024
Approved by	MuCol Management Committee	All	28/10/2024

IMCC & MuCol Authors

Carlotta Accettura[1], Simon Adrian[2], Rohit Agarwal[3], Claudia Ahdida[1], Chiara Aimé[4], Avni Aksoy[1,5], Gian Luigi Alberghi[6], Siobhan Alden[7], Luca Alfonso[8], Nicola Amapane[9,10], David Amorim[1], Paolo Andreetto[11], Fabio Anulli[12], Rob Appleby[13], Artur Apresyan[14], Pouya Asadi[15], Mohammed Attia Mahmoud[16], Bernhard Auchmann[17,1], John Back[18], Anthony Badea[19], Kyu Jung Bae[20], E.J. Bahng[21], Lorenzo Balconi[22,23], Fabrice Balli[24], Laura Bandiera[25], Carmelo Barbagallo[1], Roger Barlow[26], Camilla Bartoli[27], Nazar Bartosik[10], Emanuela Barzi[14], Fabian Batsch[1], Matteo Bauce[12], Michael Begel[28], J. Scott Berg[28], Andrea Bersani[8], Alessandro Bertarelli[1], Francesco Bertinelli[1], Alessandro Bertolin[11], Pushpalatha Bhat[14], Clarissa Bianchi[27], Michele Bianco[1], William Bishop[18,29], Kevin Black[30], Fulvio Boattini[1], Alex Bogacz[31], Maurizio Bonesini[32], Bernardo Bordini[1], Patricia Borges de Sousa[1], Salvatore Bottaro[33], Luca Bottura[1], Steven Boyd[18], Marco Breschi[27,6], Francesco Broggi[23], Matteo Brunoldi[34,4], Xavier Buffat[1], Laura Buonincontri[35,11], Philip Nicholas Burrows[36], Graeme Campbell Burt[37,38], Dario Buttazzo[39], Barbara Caiffi[8], Sergio Calatroni[1], Marco Calviani[1], Simone Calzaferri[34], Daniele Calzolari[1,11], Claudio Cantone[40], Rodolfo Capdevilla[14], Christian Carli[1], Carlo Carrelli[41], Fausto Casaburo[42,12,8], Massimo Casarsa[43], Luca Castelli[42,12], Maria Gabriella Catanesi[44], Lorenzo Cavallucci[27,6], Gianluca Cavoto[42,12], Francesco Giovanni Celiberto[45], Luigi Celona[46], Alessia Cemmi[41], Sergio Ceravolo[40], Alessandro Cerri[47,48,39], Francesco Cerutti[1], Gianmario Cesarini[40], Cari Cesarotti[49], Antoine Chancé[24], Nikolaos Charitonidis[1], mauro chiesa[4], Paolo Chiggiato[1], Vittoria Ludovica Ciccarella[40,42], Pietro Cioli Puviani[50], Anna Colaleo[51,44], Francesco Colao[41], Francesco Collamati[12], Marco Costa[52], Nathaniel Craig[53], David Curtin[54], Heiko Damerau[1], Giacomo Da Molin[55], Laura D'Angelo[56], Sridhara Dasu[30], Jorge de Blas[57], Stefania De Curtis[58], Herbert De Gersem[56], Jean-Pierre Delahaye[1], Tommaso Del Moro[42,41], Dmitri Denisov[28], Haluk Denizli[59], Radovan Dermisek[60], Paula Desiré Valdor[1], Charlotte Desponds[1], Luca Di Luzio[11], Elisa Di Meco[40], Eleonora Diociaiuti[40], Karri Folan Di Petrillo[19], Ilaria Di Sarcina[41], Tommaso Dorigo[11,61], Karlis Dreimanis[62], Tristan du Pree[63,64], Hatice Duran Yildiz[5], Thomas Edgecock[26], Siara Fabbri[1], Marco Fabbrichesi[43], Stefania Farinon[8], Guillaume Ferrand[24], Jose Antonio Ferreira Somoza[1], Max Fieg[65], Frank Filthaut[66,63], Patrick Fox[14], Roberto Franceschini[67,68], Rui Franqueira Ximenes[1], Michele Gallinaro[55], Maurice Garcia-Sciveres[3], Luis Garcia-Tabares[69], Ruben Gargiulo[42], Cedric Garion[1], Maria Vittoria Garzelli[70,71], Marco Gast[72], Lisa Generoso[51,44], Cecilia E. Gerber[73], Luca Giambastiani[35,11], Alessio Gianelle[11], Eliana Gianfelice-Wendt[14], Stephen Gibson[7], Simone Gilardoni[1], Dario Augusto Giove[23], Valentina Giovinco[1], Carlo Giraldin[11,74], Alfredo Glioti[24], Arkadiusz Gorzawski[75,1], Mario Greco[68], Christophe Grojean[76], Alexej Grudiev[1], Edda Gschwendtner[1], Emanuele Gueli[12,12], Nicolas Guilhaudin[1], Chengcheng Han[77], Tao Han[78], John Michael Hauptman[21], Matthew Herndon[30], Adrian D Hillier[29], Micah Hillman[79], Tova Ray Holmes[79], Samuel Homiller[80], Sudip Jana[81], Sergo Jindariani[14], Sofia Johannesson[75], Benjamin Johnson[79], Owain Rhodri Jones[1], Paul-Bogdan Jurj[82], Yonatan Kahn[14], Rohan Kamath[82], Anna Kario[64], Ivan Karpov[1], David Kelliher[29], Wolfgang Kilian[83], Ryuichiro Kitano[84], Felix Kling[76], Antti Kolehmainen[1], K.C. Kong[85], Jaap Kosse[17], Georgios Krintiras[85], Karol Krizka[86], Nilanjana Kumar[87], Erik Kvikne[1], Robert Kyle[88], Emanuele Laface[75], Michela Lancellotti[1], Kenneth Lane[89], Andrea Latina[1], Anton Lechner[1], Junghyun Lee[20], Lawrence Lee[79], Seh Wook Lee[20], Thibaut Lefevre[1], Emanuele Leonardi[12], Giuseppe Lerner[1], Peiran Li[90], Qiang Li[91], Tong Li[92], Wei Li[93], Mats Lindroos[†,75], Ronald Lipton[14], Da Liu[78], Miaoyuan Liu[94], Zhen Liu[90], Roberto Li Voti[42,40], Alessandra Lombardi[1], Shivani Lomte[30], Kenneth Long[82,29], Luigi Longo[44], José Lorenzo[95], Roberto Losito[1], Ian Low[96,97], Xianguo Lu[18], Donatella Lucchesi[35,11], Tianhuan Luo[3],

Anna Lupato[35,11], Yang Ma[6], Shinji Machida[29], Thomas Madlener[76], Lorenzo Magaletti[98,44,98], Marcello Maggi[44], Helene Mainaud Durand[1], Fabio Maltoni[99,27,6], Jerzy Mikolaj Manczak[1], Marco Mandurrino[10], Claude Marchand[24], Francesco Mariani[23,42], Stefano Marin[1], Samuele Mariotto[22,23], Stewart Martin-Haugh[29], Maria Rosaria Masullo[100], Giorgio Sebastiano Mauro[46], Andrea Mazzolari[25,101], Krzysztof Mękała[102,76], Barbara Mele[12], Federico Meloni[76], Xiangwei Meng[103], Matthias Mentink[1], Elias Métral[1], Rebecca Miceli[27], Natalia Milas[75], Abdollah Mohammadi[30], Dominik Moll[56], Alessandro Montella[104], Mauro Morandin[11], Marco Morrone[1], Tim Mulder[1], Riccardo Musenich[8], Marco Nardecchia[42,43], Federico Nardi[35], Felice Nenna[51,44], David Neuffer[14], David Newbold[29], Daniel Novelli[8,42], Maja Olvegård[105], Yasar Onel[106], Domizia Orestano[67,68], John Osborne[1], Simon Otten[64], Yohan Mauricio Oviedo Torres[107], Daniele Paesani[40,1], Simone Pagan Griso[3], Davide Pagani[6], Kincso Pal[1], Mark Palmer[28], Alessandra Pampaloni[8], Paolo Panci[39,108], Priscilla Pani[76], Yannis Papaphilippou[1], Rocco Paparella[23], Paride Paradisi[35,11], Antonio Passeri[68], Jaroslaw Pasternak[82,29], Nadia Pastrone[10], Antonello Pellecchia[44], Fulvio Piccinini[4], Henryk Piekarz[14], Tatiana Pieloni[109], Juliette Plouin[24], Alfredo Portone[95], Karolos Potamianos[18], Joséphine Potdevin[109,1], Soren Prestemon[3], Teresa Puig[110], Ji Qiang[3], Lionel Quettier[24], Tanjona Radonirina Rabemananjara[111,63], Emilio Radicioni[44], Raffaella Radogna[51,44], Ilaria Carmela Rago[12], Andris Ratkus[62], Elodie Resseguie[3], Juergen Reuter[76], Pier Luigi Ribani[27], Cristina Riccardi[34,4], Stefania Ricciardi[29], Tania Robens[112], Youri Robert[1], Chris Rogers[29], Juan Rojo[63,111], Marco Romagnoni[101,25], Kevin Ronald[88,38], Benjamin Rosser[19], Carlo Rossi[1], Lucio Rossi[22,23], Leo Rozanov[19], Maximilian Ruhdorfer[113], Richard Ruiz[114], Saurabh Saini[47,1], Filippo Sala[27,6], Claudia Salierno[27], Tiina Salmi[115], Paola Salvini[4,34], Ennio Salvioni[47], Nicholas Sammut[116], Carlo Santini[23], Alessandro Saputi[25], Ivano Sarra[40], Giuseppe Scarantino[23,42], Hans Schneider-Muntau[117], Daniel Schulte[1], Jessica Scifo[41], Tanaji Sen[14], Carmine Senatore[118], Abdulkadir Senol[59], Daniele Sertore[23], Lorenzo Sestini[11], Ricardo César Silva Rêgo[107,119], Federica Maria Simone[98,44], Kyriacos Skoufaris[1], Gino Sorbello[120,46], Massimo Sorbi[22,23], Stefano Sorti[22,23], Lisa Soubirou[24], David Spataro[76], Farinaldo S. Queiroz[107,119], Anna Stamerra[51,44], Steinar Stapnes[1], Giordon Stark[121], Marco Statera[23], Bernd Michael Stechauner[122,1], Shufang Su[123], Wei Su[77], Xiaohu Sun[91], Alexei Sytov[25], Jian Tang[77], Jingyu Tang[124,103], Rebecca Taylor[1], Herman Ten Kate[64,1], Pietro Testoni[95], Leonard Sebastian Thiele[2,1], Rogelio Tomas Garcia[1], Max Topp-Mugglestone[1,36], Toms Torims[62,1], Riccardo Torre[8], Luca Tortora[68,67], Ludovico Tortora[68], Sokratis Trifinopoulos[49], Sosoho-Abasi Udongwo[2,1], Ilaria Vai[34,4], Riccardo Umberto Valente[23], Ursula van Rienen[2], Rob Van Weelderen[1], Marion Vanwelde[1], Gueorgui Velev[14], Rosamaria Venditti[51,44], Adam Vendrasco[79], Adriano Verna[41], Gianluca Vernassa[1,125], Arjan Verweij[1], Piet Verwilligen[44], Yoxara Villamizar[107,126], Ludovico Vittorio[127], Paolo Vitulo[34,4], Isabella Vojskovic[75], Dayong Wang[91], Lian-Tao Wang[19], Xing Wang[128], Manfred Wendt[1], Markus Widorski[1], Mariusz Wozniak[1], Yongcheng Wu[129], Andrea Wulzer[130,131], Keping Xie[78], Yifeng Yang[132], Yee Chinn Yap[76], Katsuya Yonehara[14], Hwi Dong Yoo[133], Zhengyun You[77], Marco Zanetti[35], Angela Zaza[51,44], Liang Zhang[88], Ruihu Zhu[134,135], Alexander Zlobin[14], Davide Zuliani[35,11], José Francisco Zurita[136]

[1] *CH - CERN*
[2] *DE - UROS, University of Rostock*
[3] *US - LBL, Lawrence Berkely National Laboratory*
[4] *IT - INFN - Pavia, Istituto Nazionale di Fisica Nucleare Sezione di Pavia*
[5] *TR - Ankara University*
[6] *IT - INFN - Bologna, Instituto Nazionale Di Fisica Nucleare - Sezione di Bologna*
[7] *UK - RHUL, Royal Holloway and Bedford New College*
[8] *IT - INFN - Genova, Istituto Nazionale di Fisica Nucleare Sezione di Genova*

[9] *IT - UNITO, Università di Torino*
[10] *IT - INFN - Torino, Istituto Nazionale di Fisica Nucleare Sezione di Torino*
[11] *IT - INFN - Padova, Istituto Nazionale di Fisica Nucleare Sezione di Padova*
[12] *IT - INFN - Roma, Istituto Nazionale di Fisica Nucleare Sezione di Roma*
[13] *UK - UOM, University of Manchester*
[14] *US - FNAL, Fermi National Accelerator Laboratory - Fermilab*
[15] *US - UO, University of Oregon*
[16] *EG - CHEP-FU, Center of High Energy Physics, Fayoum University*
[17] *CH - PSI, Paul Scherrer Institute*
[18] *UK - UWAR, The University of Warwick*
[19] *US - UChicago, University of Chicago*
[20] *KR - KNU, Kyungpook National University*
[21] *US - ISU, Iowa State University*
[22] *IT - UMIL, Università degli Studi di Milano*
[23] *IT - INFN - Milano, Istituto Nazionale di Fisica Nucleare Sezione di Milano*
[24] *FR - CEA, Commissariat à l'Energie Atomique*
[25] *IT - INFN - Ferrara, Istituto Nazionale di Fisica Nucleare Sezione di Ferrara*
[26] *UK - HUD, University of Huddersfield*
[27] *IT - UNIBO, Università degli Studi di Bologna*
[28] *US - BNL, Brookhaven National Laboratory*
[29] *UK - RAL, Rutherford Appleton Laboratory*
[30] *US - University of Wisconsin-Madison*
[31] *US - JLAB, Jefferson Laboratory*
[32] *IT - INFN - Milano Bicocca, Istituto Nazionale di Fisica Nucleare Sezione di Milano Bicocca*
[33] *IL - TAU, Tel Aviv University*
[34] *IT - UNIPV, Università degli Studi di Pavia*
[35] *IT - UNIPD, Università degli Studi di Padova*
[36] *UK - UOXF, University of Oxford*
[37] *UK - ULAN, University of Lancaster*
[38] *UK - CI, The Cockcroft Institute*
[39] *IT - INFN - Pisa, Instituto Nazionale Di Fisica Nucleare - Sezione di Pisa*
[40] *IT - INFN - Frascati, Istituto Nazionale di Fisica Nucleare - Laboratori Nazionali di Frascati*
[41] *IT - ENEA, Agenzia Nazionale per le nuove tecnologie, l'energia e lo sviluppo economico sostenibile*
[42] *IT - Sapienza, Università degli Studi di Roma "La Sapienza"*
[43] *IT - INFN - Trieste, Istituto Nazionale di Fisica Nucleare Sezione di Trieste*
[44] *IT - INFN - Bari, Instituto Nazionale Di Fisica Nucleare - Sezione di Bari*
[45] *ES - UAH, Universidad de Alcalá*
[46] *IT - INFN - LNS, Istituto Nazionale di Fisica Nucleare - Laboratori Nazionali del Sud*
[47] *UK - UOS, The University of Sussex*
[48] *IT - UNISI, Università degli Studi di Siena*
[49] *US - MIT, Massachusetts Institute of Technology*
[50] *IT - POLITO, Politecnico di Torino*
[51] *IT - UNIBA, University of Bari*
[52] *CA - PITI, Perimeter Institute for Theoretical Physics*
[53] *US - UC Santa Barbara, University of California, Santa Barbara*
[54] *CA - U of T, University of Toronto*
[55] *PT - LIP, Laboratorio de instrumentacao e Fisica Experimental De Particulas*
[56] *DE - TUDa, Technische Universität Darmstadt*
[57] *ES - UGR, Universidad de Granada*
[58] *IT - INFN - Firenze - Istituto Nazionale di Fisica Nucleare - Sezione di Firenze*
[59] *TR - IBU, Bolu Abant Izzet Baysal University*
[60] *US - IU Bloomington, Indiana University Bloomington*

[61] *SE - LTU, Luleå University of Technology*
[62] *LV - RTU, Riga Technical University*
[63] *NL - Nikhef, Dutch National Institute for Subatomic Physics*
[64] *NL - UTWENTE, University of Twente*
[65] *US - UC Irvine, University of California, Irvine*
[66] *NL - RU, Radboud University*
[67] *IT - UNIROMA3, Università degli Studi Roma Tre*
[68] *IT - INFN - Roma 3, Istituto Nazionale di Fisica Nucleare Sezione di Roma Tre*
[69] *ES - CIEMAT, Centro de Investigaciones Energéticas, Medioambientales y Tecnológicas*
[70] *DE - Uni Hamburg, Universität Hamburg*
[71] *IT - UNICA, Università di Cagliari*
[72] *DE - KIT, Karlsruher Institut Fur Technologie*
[73] *US - UIC Physics, Department of Physics, University of Illinois Chicago*
[74] *IT - UNIPD, Università degli Studi di Padova*
[75] *SE - ESS, European Spallation Source ERIC*
[76] *DE - DESY, Deutsches Elektronen Synchrotron*
[77] *CN - SYSU, Sun Yat-Sen University*
[78] *US - Pitt PACC, Pittsburgh Particle Physics, Astrophysics and Cosmology Center*
[79] *US - UT Knoxville, University of Tennessee, Knoxville*
[80] *US - Harvard University*
[81] *DE - MPIK, Max-Planck-Institut für Kernphysik*
[82] *UK - Imperial College London*
[83] *DE - Uni Siegen, Universität Siegen*
[84] *JP - KEK, High Energy Accelerator Research Organization*
[85] *US - KU, University of Kansas*
[86] *UK - University of Birmingham*
[87] *IN - SGT U, Shree Guru Gobind Singh Tricentenary University*
[88] *UK - STRATH, University of Strathclyde*
[89] *US - BU, Boston University*
[90] *US - UMN, University of Minnesota*
[91] *CN - PKU, Peking University*
[92] *CN - NKU, Nankai University*
[93] *US - Rice University*
[94] *US - Purdue University*
[95] *ES - F4E, Fusion For Energy*
[96] *US - Northwestern, Department of Physics and Astronomy, Northwestern University*
[97] *US - HEP ANL, High Energy Physics Division, Argonne National Laboratory*
[98] *IT - POLIBA, Politecnico di Bari*
[99] *BE - UCLouvain, Université Catholique de Louvain*
[100] *IT - INFN - Napoli, Istituto Nazionale di Fisica Nucleare Sezione di Napoli*
[101] *IT - UNIFE FST, Dipartimento di Fisica e Scienze della Terra, Università degli Studi di Ferrara*
[102] *PL - UW, University of Warsaw*
[103] *CN - IHEP, Institute of High Energy Physics*
[104] *SE - SU, Stockholm University*
[105] *SE - UU, Uppsala University*
[106] *US - UI, University of Iowa*
[107] *BR - UFRN - IIP, Universidade Federal do Rio Grande do Norte - International Institute of Physics*
[108] *IT - UNIPI DF, Univesità di Pisa, Dipartimento di Fisica*
[109] *CH - EPFL, École Polytechnique Fédérale de Lausanne*
[110] *ES - ICMAB-CSIC, Institut de Ciencia de Materials de Barcelona, CSIC*
[111] *NL - VU, Vrije Universiteit*
[112] *HR - IRB, Institut Ruđer Bošković*

[113] *US - Cornell University*
[114] *PL - IFJ PAN, Institute of Nuclear Physics Polish Academy of Sciences*
[115] *FI - TAU, Tampere University*
[116] *MT - UM, University of Malta*
[117] *FR - CS&T, Consultations Scientifiques et Techniques, La Seyne sur Mer*
[118] *CH - UNIGE, Université de Genève*
[119] *BR - UFRN, Universidade Federal do Rio Grande do Norte*
[120] *IT - UNICT, Università di Catania*
[121] *US - SCIPP UCSC, Santa Cruz Institute for Particle Physics, University of California Santa Cruz*
[122] *AT - TUW, Technische Universität Wien*
[123] *US - UA, The University of Arizona*
[124] *CN - USTC, University of Science and Technology of China*
[125] *FR - Ecole des Mines de Saint-Etienne*
[126] *BR - CCNH UFABC, Centro de Ciências Naturais e Humanas, Universidade Federal do ABC*
[127] *FR - CNRS, Centre National de la Recherche Scientifique*
[128] *US - UC San Diego, University of California, San Diego*
[129] *CN - NNU, Nanjing Normal University*
[130] *ES - ICREA, Institució Catalana de Recerca i Estudis Avançats*
[131] *ES - IFAE, Institut de Fîsica d'Altes Energies*
[132] *UK - SOTON, University of Southampton*
[133] *KR - Yonsei University*
[134] *CN - Institute of Modern Physics, Chinese Academy of Sciences*
[135] *CN - UCAS, University of Chinese Academy of Sciences*
[136] *ES - IFIC, Instituto de Fîsica Corpuscular*

[†] *deceased*

Contents

Tables

1 Introduction

This document contains updated parameters for the MuCol study. This is the second iteration of the parameters, and is developed from the tentative parameters report of 2023 [1], with the goal of working towards the final consolidated parameters in 2025.

This preliminary collection of parameters includes high-level goals, such as the target beam parameters at different key interfaces of the collider complex. It also contains many design and schematic-based parameters that have been developed bottom-up by the teams that work on the different parts of the complex and different technologies. These parameters are already the fruit of the R&D of each team, or the goals that the team considers realistic based on their expertise and studies carried out so far. This allows for identification of further development needs to be addressed in future iterations of parameters.

1.1 Muon Collider Design

The design effort focuses on a high energy stage at 10 TeV with a luminosity of $2.1 \times 10^{35}\,\mathrm{cm}^{-2}\,\mathrm{s}^{-1}$. This will demonstrate feasibility of a high energy stage matching approximately the physics reach of a $100\,\mathrm{TeV}$ energy FCC-hh design.

This muon collider can be reached through one of two paths: either through *energy staging* to build a $3\,\mathrm{TeV}$ collider prior to the full $10\,\mathrm{TeV}$, or through *luminosity staging* to begin with the full $10\,\mathrm{TeV}$ collider, but with lower initial luminosity increased by a subsequent upgrade. This could potentially be via initially a $5\,\mathrm{GeV}$ $2\,\mathrm{MW}$ proton beam on target (Option 1), then upgrade to a $10\,\mathrm{GeV}$, $4\,\mathrm{MW}$ beam (Option 2).

1.2 Structure of the Document

The overall parameters are listed in Section 2 followed by parameters for each subsystem split by section. Figure 1.1 demonstrates the present complex subsystems, starting with the proton driver (blue) in Section 3, passing through to the front end (purple) in Section 4, the muon beam cooling (pink) in Section 5, acceleration (light red) in Section 6 and 7 and finally the collider ring (red) in Section 8. Then the Detector and Machine-Detector Interface (MDI) designs are described in Section 9 and 10 respectively. Details of underlying technologies are given in subsequent sections, including magnets (Section 11) and RF (Section 12). Collective effects throughout the complex are described in Section 13, and the radiation shielding and protection considerations throughout the complex are described in Section 14. Finally, site-specific parameters are defined, particularly for the demonstrators (Section 15) and the Rapid Cycling Synchrotrons (RCS) for CERN and Fermilab (Section 16). This document prioritises new and original parameters for each system. Many of the initial baselines values for each system consider the results of the MAP study [2].

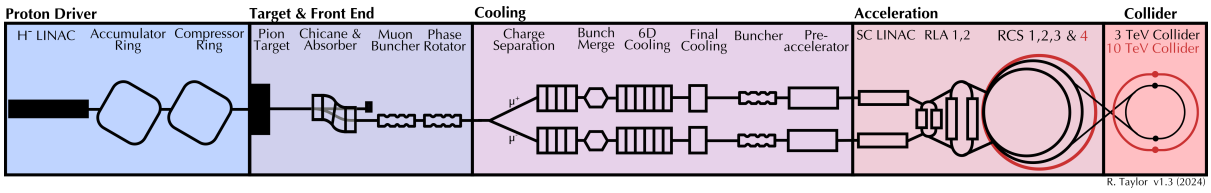

Fig. 1.1: Simplified overview of the proton driver and muon collider accelerator complex.

1.3 Differences from Tentative Parameter Report 2023

The tentative parameter set broadly assumed a new greenfield site. In reality, the facility would likely be built at an existing laboratory with significant reuse of existing infrastructure where possible. Studies to explore this opportunity are ongoing and the beginning of these results are indicated in this report within Section 16.

Studies of a muon ionisation cooling demonstrator design have begun, considering both the mechanical integration of a single cooling cell, and also the optics overview of a cooling demonstrator facility. Parameters defining the beginning of these designs are included within Section 15.

For an overview of the schedule considerations, please refer to the Tentative Parameters report [1].

2 Top-Level Parameters

The top-level parameters for the Muon Collider are shown in Table 2.1. These are the ideal design specifications that each subsystem aims to achieve. The parameters are unchanged as of last year, with an additional acknowledgement of the asymmetry in the produced μ^+, μ^- charges. Machine transmission is the ideal transmission counted after the target and capture section.
Table 2.3 provides an overview of the whole complex, with the key numbers including the length and outgoing beam energy for each sub-system. An estimate of transmission is provided, based on the current efficiency of each simulated system.

The total muon production efficiency after the front-end and cooling is $4\,\%$, which is less than the transmission budget of $10\,\%$. This discrepancy motivates the need for an increase to a $4\,\mathrm{MW}$ proton beam power to meet the intended number of muons per bunch at the collider.

Center of mass energy	Unit	3 TeV	10 TeV
Luminosity for target parameters	$10^{34}\,\mathrm{cm}^{-2}\,\mathrm{s}^{-1}$	2	20
Transverse emittance	μm	25	
Proton beam power	MW	2 - 4*	
Number of μ^+ muons per bunch	10^{12}	2.2	1.8
Number of μ^- muons per bunch	10^{12}	2.2	1.8
Target integrated luminosity	ab^{-1}	1	10
Luminosity lifetime	Turns	1039	1158
Collider peak field	T	11	16
Repetition rate	Hz	5	
Beam power	MW	5.3	14.4
Longitudinal emittance	eV s	0.025	
IP bunch length	mm	5	1.5

Table 2.1: Preliminary parameters for a muon collider at two different energies. *Currently muon transmission is not yet fully sufficient and further system design is required. As a back-up option a higher-power target can also mitigate this but affects e.g. beam loading. It should be noted that more mu+ are produced at the target, but currently we assume that this beam is collimated to have the same charge and hence the same beam loading everywhere.

Parameter	unit	after Final Cooling	Inj. at 3 TeV	Inj. at 10 TeV
Muon beam energy	GeV	0.25	1500	5000
Number of muons	10^{12}	4	2.2	1.8
Transverse norm. emittance	um	22.5	25	25
Longitudinal emittance	eVs	0.0225	0.025	0.025
RMS bunch length	mm	375	5	1.5
RMS rel. momentum spread	%	9	0.1	0.1
Av. grad (0.2GeV-1.5TeV)	MV/m		2.4	
Av. grad (1.5-5TeV)	MV/m			1.1

Table 2.2: Key target beam parameters along the collider. Gradients given are average values required to achieve the transmission target. The two cooling options under development achieve transverse emittances of 24 (29.5)μm and longitudinal values of of $0.0124(0.0289)$ eVs. The better performing one uses one solenoid with a field 25% above the current target, however we expect that reducing the field will only increase the transverse emittance, remaining below 30 μm.

Subsystem	Energy	Length	Achieved Transm.	Achieved μ^-/bunch	Target μ^-/bunch
	GeV	m	%	10^{12}	10^{12}
Proton Driver	5 (p^+)	1500	–	500 (p^+)	
Front End	0.17	150	9	45.0	
Charge Sep.	0.17	12	95	42.8	
Rectilinear A	0.14	363	50	21.4	
Bunch Merge	0.12	134	78	16.7	
Rectilinear B	0.14	424	32	5.3	
Final Cooling	0.005	100	60	3.2	
Pre-Acc.	0.25	140	86	2.8	4.0
Low-Energy Acc.	5	–	*90**	2.5	
RLA2	62.5	∘2430	90	2.3	
RCS1	314	∘5990	90	2.1	
RCS2	750	∘5990	90	1.9	
RCS3	1500	∘10700	90	1.7	
3 TeV Collider	1500	∘4500	–	1.7	2.2
RCS4	5000	∘35000	90	1.5	
10 TeV Collider	5000	∘10000	–	1.5	1.8

Table 2.3: Preliminary beam parameters at the end of each section of the acceleration chain for the 2 MW target. Lengths are approximate and ∘ indicates that the length refers to the circumference. Muon numbers in the muon cooling systems refer to the yields from Option 1 as per Table 4.4. For μ^+ the charge at the Front End is 60×10^{12} but we assume that this is reduced by collimation to provide the same bunch charge and beamloading in both beams. Currently, the achieved muon transmission is lower than the target value in the cooling and somewhat higher than the target value in the muon accelerator part. Further improvement is expected. A 4 MW target would provide almost twice as many muons at the beginning. * For the initial muon acceleration no design exists at this moment, the target value is given.

3 Proton Driver

This section is devoted to the Proton Complex parameters choice. The parameters are preliminary and based on previous studies as the MAP [2] and the Design for a Neutrino Factory at CERN [3, 4, 5] as well as simulations and studies carried out during the years of the project.

The proton driver of a future Muon Collider is required to deliver a proton-beam of at least 2 MW at a repetition rate of 5 Hz to the pion-production target. The proton-beam energy must be in the multi-GeV range in order to maximize the pion yield. In addition, a particular time structure consisting of a single very short bunch, of rms pulse length on the order of 2 ns, is needed to allow the muon beam to be captured efficiently in the cooling section. The proton bunch parameters are intimately connected and constrained by beam loading and longitudinal acceptance in the downstream muon accelerator systems and by the acceptance (in time, energy, and power) of the target and pion capture system. The proton beam parameters necessary to produce the desired number of muons in the final storage rings of the Muon Collider are listed in Tables 3.1 and 3.3. Option 1 considers a 5 GeV proton beam with a power of 2 MW, and Option 2 considers a higher energy and higher power proton beam of 10 GeV and 4 MW. These two options are equivalent to the luminosity scaling options.

Parameters	Unit	Option 1	Option 2
Final energy	GeV	5	10
Repetition rate[1]	Hz	5	
Max. source pulse length[2]	ms	3.4	5.0
Max. source pulse current[2]	mA	80.0	
Source norm. emittance	mm.mrad	0.25	
Power	MW	2	4
RF frequency	MHz	352 and 704	

Table 3.1: H- LINAC parameters for both options considering 1) LINAC single use for muon production, 2) Chopping will later reduce the average current.

The baseline proton driver design for the MuCol project is composed of a final energy multi-GeV H^- LINAC followed by two rings, a compressor and an accumulator as shown in Fig. 3.1, both operating at fixed energy. It is likely that the two lattices will be part of the same ring or tunnel. Depending on the final energy a single or a double bunch will be used with the latter needing a recombination line before reaching the target.

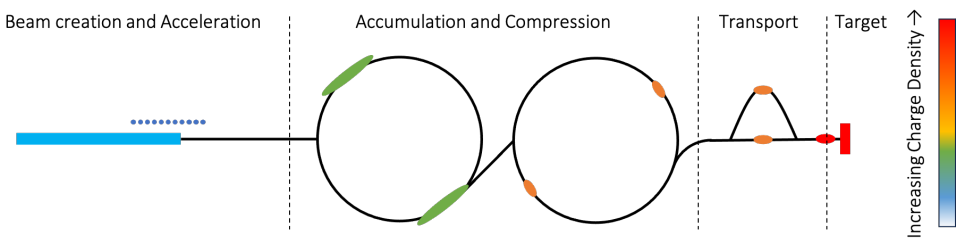

Fig. 3.1: Schematic of the baseline design for the Proton Complex.

3.1 High power Linac

The linear accelerator is the first stage of any hadron accelerator complex. The LINAC generates the initial transverse and longitudinal beam emittances and energy spread, defining the beam quality for the next stages of acceleration, accumulation and compression. For a project like the Muon Collider, where the repetition rate is low, a high-energy high-power LINAC can be a versatile machine that can serve many other purposes including (and not restricted to) neutrino factories and nuclear science experiments.

The main parameters for a Muon Collider LINAC based injector are listed in Tab. 3.1 consisting of two options that will drive the final power of the facility. For the preliminary parameters of the proton complex we will assume that the LINAC final energy of 5 GeV or 10 GeV is also the final beam energy, removing the need of further acceleration in an intermediary storage ring.

Additional components required for the proton driver includes a H^- source for charge-exchange injection, and a low-energy chopper. Linac4 at CERN could be used as the first part of a CERN based proton drive and its development and design will be used as the reference for the initial parameters of the protons. The current ongoing development of Linac4 beam studies and H^- source will be beneficial to this project, as well as any advances in source design and R&D in development[6]. A 80 mA and 1 ms pulse is needed from the source to achieve the final target chargehowever chopping has not yet been taken into account. Fig. 3.2 presents a chopping scheme for each of the options where the source current of 80 mA is assumed and a pulse length from the source of either 3.4 of 4.7 ms is needed. The pulse length is long for a H^- source, but an option of two sources working in parallel would have parameters close to current working sources.

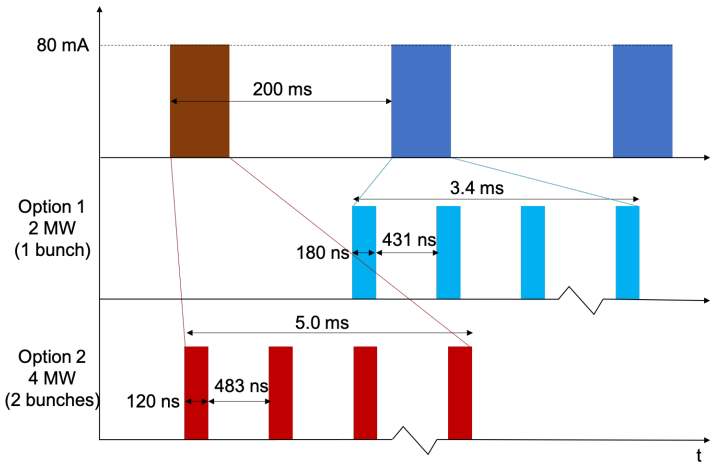

Fig. 3.2: Possible Chopping scheme for the LINAC considering a single bunch option as the baseline design.

A study on the losses in the high energy section of a full energy LINAC for both options was carried out [7]. The main contributor is black body radiation losses which indicates that the warm sections outside cryomodules and the transfer line to the accumulator ring will have to be cooled to temperatures below 200 K in order to maintain the losses within acceptable levels.

3.2 Accumulator

In order to test the stability and possible accumulation schemes for the beam coming from the LINAC we used two lattices developed for the Neutrino Factory at CERN [3, 4] and based on the parameters listed in Tab. 3.2. For both final energies no instabilities are seen throughout the turns needed for accumulation. The total tune spread due to space charge forces is 0.15 for the 5 GeV (2 MW) option and less than 0.05 for the 10 GeV (4 MW) option.

Parameters	Unit	Option 1	Option 2
Energy	GeV	5	10
Circumference	m	180	300
Final rms bunch length	ns	180	120
Geo. rms. emittance	π.mm.mrad	5.0	
Number of bunches	–	1	2
Number of turns	–	5600	5900

Table 3.2: Accumulator ring parameters

3.3 Compressor

A 10 GeV compressor lattice was developed, show in Fig. 3.3 where the 5 GeV option keeps the old lattice as developed for the Neutrino Factory at CERN [5]. Both lattices contain negative bends to minimize the momentum compaction factor while controlling the dispersion function along the ring. For both final energy options studies of the compression were carried out, including space-charge effects. The final tentative parameters for each option are listed in Tab. 3.3.

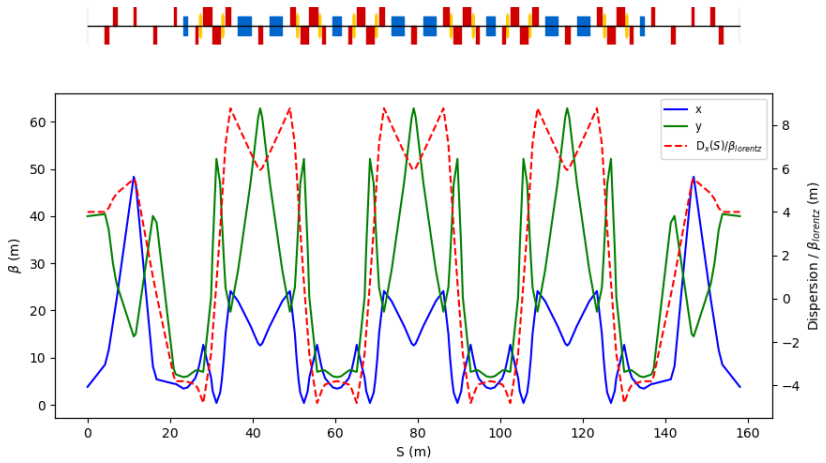

Fig. 3.3: 1 period of the compressor lattice with negative bending magnets for the 10 GeV case.[5].

For both final energies a full rotation simulation was performed and the final results are displayed in Fig. 3.4 where the sub 2 ns rms bunch length is achieved.

Parameters	Unit	Option 1	Option 2
Energy	GeV	5	10
Circumference	m	300	600
Protons on target	10^{14}	5.0	
Final rms bunch length	ns	2.0	
Geo. rms. emittance	π.mm.mrad	5.0	
RF voltage	MV	1	4
RF harmonic	–	1	2
Number of turns	–	60	70

Table 3.3: Compressor ring parameters

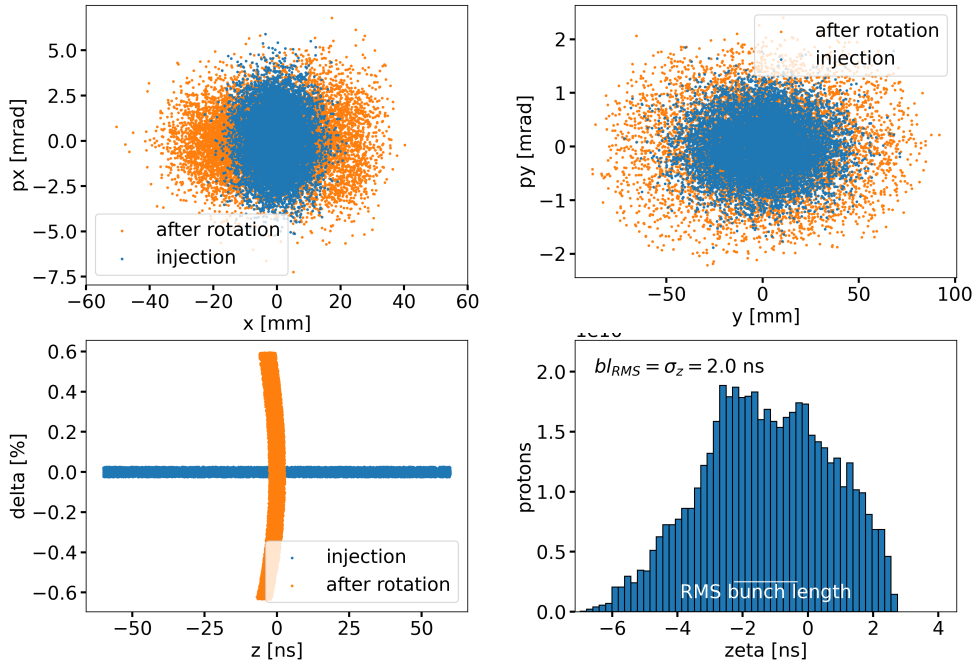

Fig. 3.4: The figure shows the 6D phase space of a bunch at injection and after rotation in the proposed 10GeV compressor lattice. The longitudinal profile along the bunch is also plotted after rotation.

3.4 Target delivery system

After rotation, the short bunch (or bunches) from the compressor have to be transported to the target. The simple transfer line was designed and simulations of the beam transport for both options were carried out, not yet taking into account the extraction line from the compressor ring. No significant degradation of the bunch length was observed, however losses were observed due to the halo from the compressor. The maximum quadrupole gradients, including the triplet needed for the final focusing on the target surface, are between 30 – 40 T/m depending on the beam final energy. Figure 3.5 shows an example of the result for a transport simulation of the compressed beam to the target surface.

3.5 Next Steps

The LINAC simulations including the chopper and accumulator ring injection studies have yet to be finalized. A study on other possible alternative compressor lattices with slower rotation and flexible slip factor, like the JPARC RCS and Main ring, is needed. A slower rotation makes the RF requirements less

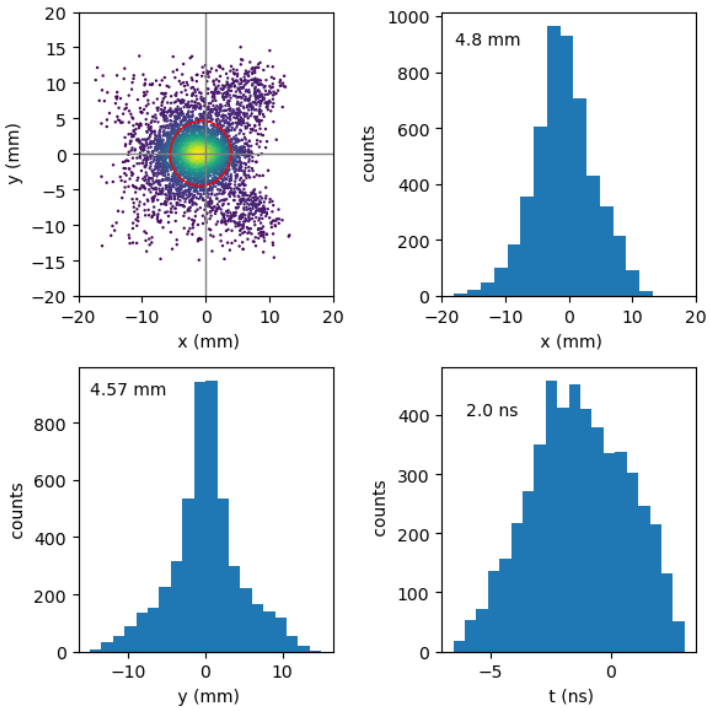

Fig. 3.5: Beam Profile and bunch length on the target surface for the 10 GeV case. The values marked on the histogram are the rms trasnverse beam sizes and bunch length.

stringent and not having negative bends also make for weaker dipole fields, making the lattice easier to tune and cheaper to manufacture. Significant beam loss was observed at the end of rotation that has to be investigated. The study of the extraction line from the accumulation, transport and recombination should be initiated for the double bunch option.

Losses in the Proton Complex will need to be studied in detail since they cause activation of elements and make maintenance complex. The budget on the LINAC is taken from the main working machine as 1 W/m however for the rings and transport line downstream there was no in depth study so far. Injection and extraction regions are of high importance as well as halo formation of formation around the beam due to space charge effects.

4 Target & Front-End

The front end of the muon collider comprises several sub-systems:

1. The target and solenoid (transverse) capture system, initially with field 15–20 T tapering to 1–2 T, in Section 4.1;
2. Extraction line for the spent proton beam in Section 4.2.2;
3. Solenoid chicane and proton absorber, in Section 4.2.1;
4. Longitudinal drift;
5. Sequence of RF cavities for bunching, in Section 4.3;
6. Further sequence of RF cavities for rotating in energy-phase space, also in Section 4.3.

These parameters are consistent with a $2\,\mathrm{MW}$, $5\,\mathrm{GeV}$ proton beam (Option 1), with the $4\,\mathrm{MW}$, $10\,\mathrm{GeV}$ (Option 2) design currently under active study.

4.1 Target and solenoid

Pions are produced by sending protons onto a graphite target immersed in a strong magnetic field. Solenoid parameters are listed in Table 11.1 of subsection 11.3.1. In the MAP design, resistive magnets (RC1–RC5) were considered, however IMCC is developing a full HTS-based alternative. The target and target systems are under design, thus no details regarding the expected operation temperature, mechanical response and life-time are listed here.

Moreover, small discrepancies exist in the components dimensions reported in this chapter, particularly between pion/muon yield studies and design and engineering calculations.

Information on the radiation load on the target solenoids is within Subsec. 14.1.

4.1.1 Production target and beam parameters

The deep inelastic interactions of the proton beam with the target produces kaons and pions, which eventually decay into muons. To capture the produced particles and keep the emittance under control, the production target and the subsequent line has to be kept in a strong solenoidal magnetic field, which confines the charged particles along helicoidal trajectories.

The baseline case considers a graphite target as the most suitable option. This material allows operation at high temperatures and has a high thermal-shock resistance. Therefore the majority of studies performed to optimize the pion-yield and estimate the radiation load on the front-end magnets have taken this target as baseline. Nevertheless, it is worth acknowledging the ongoing parallel studies for a fluidised tungsten powder target and for a liquid lead target, which will be detailed in the future.

An overview of the proton driver parameters being used in the studies of the front-end target systems is shown in Table 4.1. Different ranges of these parameters have been considered in order to optimise both the physics and engineering design.

4.1.2 Production target engineering parameters

As depicted in Table 4.2, the target system is divided into production target, target vessel, target shielding, target shielding vessel, proton beam window and muon beam window. The auxiliary services for

Parameters	Unit	Baseline	Range
Beam power	MW	2	1.5-3.0
Beam energy	GeV	5	2-10
Pulse frequency	Hz	5	5-50
Pulse intensity	p+ 10^{14}	5	3.7-7.5
Bunches per pulse		1	1-2
Pulse length	ns	2	1-2
Beam size	mm	5	1-1.5
Impinging angle	°	0	0-10

Table 4.1: Assumed beam from proton driver via carbon target used in studies

cooling of the target and shielding are equally part of the target system and are listed in Table 4.3. For both tables, the main dimensions, key material considerations and important design and integration features are summarized.

	Material	Box dimensions DxL [mm]	Integration
Production Target	Isostatic Graphite	D30 x L800	Rod supported with transverse CFC supports attached to cylindrical frame
Target Vessel	Titanium Grade 5	D346 x L920	Located in the bore of the Target shielding vessel.
Proton Beam Window	Beryllium	D220 x L0.25	
Muon Beam Window	Titanium Grade 5	D240 x L1	Welded on the vessel
Target Shielding	Tungsten	D x L2000	Inside Shielding Vessel. Multiple pie-like blocks stacked together with guiding rods.
Target Shielding Vessel	Stainless-Steel	D1218 x L2065	Supported by transversal beam across the cryostat of the solenoid.

Table 4.2: Baseline engineering parameters of the carbon target system

Cooling Unit	Coolant	Type	Mass Flow kg/s	Pressure bar	Integration
Target	Helium	Static / Natural convection	-	1	Surrounding target rod enclosed by windows and target vessel.
Target Vessel	Helium	Forced convection	0.5	10	Inside double wall target vessel. Routing upstream via the Solenoid bore.
Target Shielding	Helium	Forced convection	0.33	2	Inside Target shielding Vessel. Routing upstream via the Solenoid bore.

Table 4.3: Baseline engineering parameters of the carbon target auxiliary systems for 2MW.

The baseline for a 2 MW-class target consists of a solid graphite target. The graphite rod is housed within a double-walled vessel filled with a static helium atmosphere. This helium confinement facilitates the initial stage of heat removal from the graphite rod through natural convection, while raising the sublimation temperature of the graphite when compared to a vacuum environment and providing a non-erosive heat transfer medium. Forced convection cooling is then applied through the vessel's double wall using a 10 bar helium flow.

Titanium is a suitable candidate for the target vessel due to its low density (reduced interaction with produced pions and muons) and good thermal-shock resistance. However, it is required to use beryllium in proton and muon windows to guarantee a peak power density of approximately $800\,\mathrm{W/cm^3}$ and yearly DPA around 0.5. On the contrary, adopting titanium would increase these values by an order of magnitude.

The target vessel is surrounded by a helium-cooled, heavy tungsten shield, which reduces power deposition and radiation damage to the solenoid materials to acceptable levels. For details on the radiation shielding, see Section 14. The target proximity shielding is housed inside a large stainless-steel vessel, extending from just upstream of the target to around 2 meters downstream. The large size and weight, combined with the need to efficiently extract heat from each tungsten block, resulted in proximity shielding composed of multiple pie-shaped tungsten segments, perforated in specific locations to either guide helium flow or allow for the insertion of longitudinal rods to hold the assembly together. The shielding vessel also hosts a water layer to moderate the neutrons.

Both the cooling and instrumentation routing for the target systems are handled via the upstream side of the assembly.

Downstream of the target and its cooled shielding assembly, the shielding is made of tungsten and has an aperture following the parabolic shape defined in the MAP studies.

4.1.3 Muons and pions yield

To assess the most suitable conditions to operate the proton driver and to design the target, several FLUKA simulations were conducted, calculating the muon and the pion yield in each setting. For this purpose, it was assumed that all the muon and pions going in the chicane can be captured if their momentum is below $500\,\mathrm{MeV/c}$. The obtained yields are summarized as a function of beam energy in Table 4.4, assuming a transverse beam sigma of 5 mm and a graphite target rod with a radius of 15 mm.

Yield $[10^{-2}\mathrm{GeV}\ /p^{+}]$	3	4	5	6	7	8	9	10
μ^{+}	2.8	2.6	2.4	2.3	2.2	2.1	1.9	1.9
μ^{-}	1.8	1.8	1.8	1.8	1.7	1.7	1.7	1.7
π^{+}	1.3	1.2	1.1	1.1	1	0.98	0.92	0.9
π^{-}	0.84	0.81	0.84	0.82	0.83	0.8	0.8	0.81

Table 4.4: Yield per unit energy proton beam $[10^{-2}\mathrm{GeV}\ /p^{+}]$

4.1.4 Target radial build

A preliminary target radial build has been defined and is shown in Table 4.5. This build takes into account a 700 mm inner-radius solenoid coil, the baseline target system dimensions as described in Table 4.2, and the required shielding configuration with a water and Boron-Carbide neutron-absorbing layers (Table 14.1). The discrepancy in thickness of tungsten shielding between Table 4.5 and Table 14.1 is explained by the need to integrate other components in the prior as part of the exercise to engineer the entire target-solenoid cryostat.

Component	Material	r_i [mm]	r_e [mm]	Δr [mm]
Solenoid coils	HTS	700	-	-
Insulation	Insulation	690	700	10
Vacuum	Vacuum	670	690	20
Thermal shield	Copper & Water	651	670	19
Vacuum	Vacuum	631	651	20
Inner supporting tube	Stainless-steel	619	631	12
Vacuum	Vacuum	609	619	10
Outer Target shielding	Tungsten	599	609	10
Neutron absorber	Boron Carbide	594	599	5
Target shielding and neutron moderator	Stainless-steel	589	594	5
	Water	569	589	20
	Stainless-steel	564	569	5
	Tungsten	179	564	385
	Stainless-steel	174	179	5
Vacuum	Vacuum	173	174	1
Target vessel	Titanium	168	173	5
	Helium	155	168	13
	Titanium	150	155	5
	Helium	15	150	135
Target	Graphite	0	15	15

Table 4.5: Target System radial build for a graphite target.

4.2 Front-End

4.2.1 Chicane and proton absorber

The target solenoid is followed by a solenoid chicane which is terminated by a thick beryllium cylinder. The cylinder absorbs low energy remnant protons which would otherwise irradiate equipment downstream of the chicane. The concept was initially introduced in [8] and initial parameters were defined. Further discussion was made in [9]. In particular, the former study assumed $1.5\,\mathrm{T}$ solenoid fields, while the MAP and latter study considered $2\,\mathrm{T}$ solenoid fields in this region. The latter study also noted that a large proportion of undecayed pions were stopped in the proton absorber which negatively impacted the muon yield.

Table 4.6 shows the current design parameters for the chicane and the proton absorber.

Parameters	Unit	Value
Chicane bend angle	degree	15
Chicane radius of curvature	m	22
Proton absorber material	-	Be
Proton absorber thickness	m	0.1
Chicane field	T	1.5

Table 4.6: Chicane and proton absorber parameters

4.2.2 Spent proton beam extraction

A non-negligible fraction of the primary protons do not have an inelastic nuclear collision in the production target and escape from the graphite rod. At these energies, the protons are not bent significantly

by the chicane and would be lost on the chicane aperture. In absence of a mitigation strategy, the energy carried by these particles would lead to a high power deposition density in the normal-conducting chicane solenoids. In addition, a high cumulative ionizing dose and displacement damage would be reached within a short operational time. It is therefore necessary to extract the spent protons from the front-end and steer them onto an external beam dump.

Earlier studies explored a possible solution of injecting the proton beam at different angles into the front-end, with an extraction channel envisaged in a gap between the superconducting magnets upstream of the chicane. This concept proved to be unfeasible due to geometrical aspects and the increase of the radiation load to the superconducting coils. As an alternative solution, the spent proton beam could be extracted in the middle of the chicane, by using solenoids with different diameters in order to create a gap for the high-energy protons. Shower simulation studies showed that such an extraction channel in the chicane needs to have a transverse size of a few tens of centimeters, which is challenging for the magnet design. In addition, an internal radiation shielding would be needed to protect the coils from particles, which are still lost in the chicane. The chicane design studies are presently still ongoing.

Parameters	Unit	
Num. micro bunches		21
Longit. emittance	mm	46
Transv. emittance	um	17000
Positive muon yield	1/GeV per p+	0.024
Negative muon yield	1/Gev per p+	0.018

Table 4.7: Outgoing muon beam

4.3 Buncher & Phase Rotator

The buncher is comprised of a sequence of RF cavities. The cavity frequency is chosen to match the distance between nominal RF bunches, so that it varies along the length of the buncher. The phase is purely bunching.

In the phase rotator, cavities are dephased so that the low energy tail of the beam sees an accelerating gradient and the high energy front of the beam sees a decelerating gradient.

Cavities are placed in a two-cavity LINAC with $0.25\,\mathrm{m}$ separation between adjacent cavity pairs. Each cavity in the pair is independently phased. Transversely, the beam is contained in a $2\,\mathrm{T}$ field.

5 Cooling

The cooling channel is defined from the end of the RF capture system to the beginning of acceleration. Five sub-systems are part of the cooling apparatus:

1. Charge separation, which splits the positive and negative muon species into separate beamlines;
2. Rectilinear cooling (A and B lattices) which cools the beam in 6D phase space;
3. Bunch merge after the A lattice merges the microbunches produced by the front end into a single bunch;
4. Final cooling, which produces the final low emittance beam;
5. Re-acceleration, which accelerates the low energy beam up to 200 MeV/c.

For this first iteration, parameters are listed in Table 5.1 for the principal subsystems: rectilinear cooling and final cooling. Additional details are available for the charge separation [10] and bunch merge [11] subsystems. Potential performance for re-acceleration is estimated.

Num. bunches Unit	Actual ε_{T} um	Target ε_{T} um	Actual ε_{L} mm (eVs)	Target ε_{L} mm (eVs)	Mean p_z MeV/c	Transm. %
End of charge separation	-	17000	-	46	288	95.0
6D Cooling end of **Stage 8**	260	300	1.86	1.5	200	14.9
End of Final Cooling	29.5	22.5	82 (0.0289)	64	50	4.0
End of Reacceleration	-	22.5	-	64 (0.0225)	339	3.8

Num. bunches Unit	Actual ε_{T} um	Target ε_{T} um	Actual ε_{L} mm (eVs)	Target ε_{L} mm (eVs)	Mean p_z MeV/c	Transm. %
6D Cooling end of **Stage 10**	140	140	1.56	1.56	200	10.5
End of high field Final Cooling	24	22.5	35.3	64	36.4	6.3
End of Reacceleration	-	22.5	-	64 (0.0225)	339	5.9

Table 5.1: Beam parameters entering and leaving the cooling system for short-rectilinear (top) and long-rectilinear (bottom) options. The target emittances are listed. They are 10 % more demanding than the nominal emittances in the RCS and collider, allowing for some emittance growth at some point in the acceleration chain.

5.1 Rectilinear Cooling

The rectilinear cooling section consists of a number of solenoid magnets with dipole field superimposed. In the MAP design the dipole field was achieved by means of introducing a tilt in the solenoids but separate dipoles are proposed for this IMCC design. The rectilinear cooling lattice described below is stored in the MuonCollider-WG4 github group, `rectilinear` repository as release (branch) `2024-09-27_release` and described in [12].

The solenoid field is approximately sinusoidal with a period given by the cell length L so that $B_z(z, r = 0) = B_{peak} \sin(2\pi z/L)$. Cells in the Rectilinear B lattices are increasingly non-sinusoidal, with a component $B_z(z, r = 0) = B_{peak} \sin(4\pi z/L)$ that gets stronger further down the B lattice. The peak B_z listed in Table 5.3 is the peak field on the axis of the solenoid. Fields may be higher in the conductor volume.

RF cavities are modelled as perfect cylindrical pillbox cavities operating in TM010 mode. Several RF cavities are included within each cell. A thin conductive window electromagnetically seals the RF cavities so that the pillbox model is an adequate approximation to the real cavity field and the cavities can be assumed to be independently phased. The RF gradient listed in Table 5.4 is the peak gradient.

Updates for the A and B stages of the rectilinear cooling system have been developed, comprising of 10 "B-type" stages, denoted S1 through S10 that yields improved performance over the MAP lattice listed above and has been designed using 352 MHz RF and harmonics. The performance is summarised in Table 5.2.

Hardware parameters are described in Table 5.3. In this lattice, the dipoles were simulated as a magnet independent of the solenoids which were not tilted and the dipole field is listed.

	ε_T mm	ε_L mm	ε_{6D} mm^3	Stage Transmission	Cumulative Transmission %
Start	16.96	45.53	13500		100
A-Stage 1	5.17	18.31	492.60	75.2	75.2
A-Stage 2	2.47	7.11	44.03	84.4	63.5
A-Stage 3	1.56	3.88	9.59	85.6	54.3
A-Stage 4	1.24	1.74	2.86	91.3	49.6
Bunch merge	5.13	9.99	262.5	78.0	38.7
B-Stage 1	2.89	9.09	76.07	85.2	33.0
B-Stage 2	1.99	6.58	26.68	89.4	29.4
B-Stage 3	1.27	4.05	6.73	87.5	25.8
B-Stage 4	0.93	3.16	2.83	89.8	23.2
B-Stage 5	0.70	2.51	1.32	89.4	20.7
B-Stage 6	0.48	2.29	0.55	88.4	18.2
B-Stage 7	0.39	2.06	0.31	92.8	17.0
B-Stage 8	0.26	1.86	0.13	87.9	14.9
B-Stage 9	0.19	1.72	0.06	85.2	12.7
B-Stage 10	0.14	1.56	0.03	87.1	11.1

Table 5.2: Rectilinear cooling performance in terms of emittance reduction (transverse, longitudinal and 6D) and transmission per stage.

	Cell Length m	Stage Length m	Pipe Radius cm	Max. B_z On-Axis T	Int. B_y Tm	$\beta_\perp$ cm	D_x mm	On-Axis Wedge Len. cm	Wedge Angle deg
A-Stage 1	1.8	104.4	28	2.5	0.102	70	-60	14.5	45
A-Stage 2	1.2	106.8	16	3.7	0.147	45	-57	10.5	60
A-Stage 3	0.8	64.8	10	5.7	0.154	30	-40	15	100
A-Stage 4	0.7	86.8	8	7.2	0.186	23	-30	6.5	70
B-Stage 1	2.3	50.6	23	3.1	0.106	35	-51.8	37	110
B-Stage 2	1.8	66.6	19	3.9	0.138	30	-52.4	28	120
B-Stage 3	1.4	84.0	12.5	5.1	0.144	20	-40.6	24	115
B-Stage 4	1.2	66.0	9.5	6.6	0.163	15	-35.1	20	110
B-Stage 5	0.8	44.0	6	9.1	0.116	10	-17.7	12.5	120
B-Stage 6	0.7	38.5	4.5	11.5	0.087	6	-10.6	11	130
B-Stage 7	0.7	28.0	3.75	13	0.088	5	-9.8	10	130
B-Stage 8	0.65	46.15	2.85	15.8	0.073	3.8	-7	7	140
B-Stage 9	0.65	33.8	2.3	16.6	0.069	3	-6.1	7.5	140
B-Stage 10	0.63	29.61	2.0	17.2	0.069	2.7	-5.7	6.8	140

Table 5.3: Rectilinear cooling cell hardware in terms of cell geometry, solenoid fields, dipole fields and wedge geometry

	RF Frequency MHz	Num. RF	RF Length cm	Max. RF Gradient MV/m	RF phase deg
A-Stage 1	352	6	19	27.4	18.5
A-Stage 2	352	4	19	26.4	23.2
A-Stage 3	704	5	9.5	31.5	23.7
A-Stage 4	704	4	9.5	31.7	25.7
B-Stage 1	352	6	25	21.2	29.9
B-Stage 2	352	5	22	21.7	27.2
B-Stage 3	352	4	19	24.9	29.8
B-Stage 4	352	3	22	24.3	31.3
B-Stage 5	704	5	9.5	22.5	24.3
B-Stage 6	704	4	9.5	28.2	22.1
B-Stage 7	704	4	9.5	28.5	18.4
B-Stage 8	704	4	9.5	27.1	14.5
B-Stage 9	704	4	9.5	29.7	11.9
B-Stage 10	704	4	9.5	24.9	12.2

Table 5.4: Rectilinear cooling cell RF parameters. 0^o phase is bunching mode.

5.2 Final cooling (short rectilinear)

A 75 m long final cooling system has been developed and optimised with RF-Track. This system is made of 11 cells, each of which is composed of a high-field ≈40 T solenoid which encompasses a liquid or gaseous hydrogen absorbers, and a long low-field solenoid which encompasses a series of RF cavities and their drift regions. The RF cavities are split into acceleration, to restore the energy lost from the absorber, and rotation, to restore a more uniform momentum distribution of the beam. The beam conditions at the start of Cell 1 for this design were assumed based on previous rectilinear cooling cell designs from MAP; they are approximately compatible with the end of rectilinear B-8.

The hardware parameters for the final cooling cells, and the final cooling RF cavities are in Table 5.6 and 5.7 respectively.

The performance of this system is sufficient to reach 29.5 µm in transverse emittance ε_T, which is 4.5 µm away from the target emittance of 25 µm. The longitudinal emittance ε_L increases from 2.7 mm to 82 mm, which is significantly larger than the target emittance of 64 mm. However the transmission does not presently meet the target, as only 28.5 % of the beam remains, due to both decays and losses within the absorbers. An optimisation effort is ongoing to improve the capture of beam within the RF buckets and therefore have reasonable transmission throughout the cooling channel. Matching coils between high and low field regions are required to prevent emittance blow-up due to mismatches.

Cell no.	ε_T µm	ε_L mm	ε_{6D} µm	Cumulative transmission %
Start	300	1.5		100
1	275.2	2.7	586.1	97.5
2	212.7	5.9	645.4	94.1
3	170.4	6.8	582.8	88.9
4	138	12.4	617.5	81.9
5	102.5	20.6	600	74.4
6	81.3	25	548.8	61.1
7	59.5	32.7	486.9	53.1
8	50.8	43.6	482.8	46.9
9	41.2	48.4	434.2	37
10	32.9	66.1	414.6	31.7
11	29.5	82	414.5	28.5

Table 5.5: Baseline final cooling performance in terms of emittance reduction (transverse, longitudinal and 6D) and cumulative transmission per stage.

Cell no.	Solenoid length m	Stage length m	Max. B_z on-axis T	Low B_z on-axis T	Absorber length m
1	1.48	1.48	44.63	4.63	0.85
2	1.75	4.57	44.63	4.63	0.47
3	1.00	6.61	44.63	4.63	0.47
4	1.00	7.75	44.63	4.63	0.40
5	1.00	5.09	44.63	4.63	0.30
6	1.11	6.86	44.63	4.63	0.25
7	1.33	7.06	42.00	2.00	0.30
8	0.80	6.70	42.00	2.00	0.10
9	1.48	8.37	41.00	1.00	0.17
10	0.95	6.76	40.80	0.80	0.08
11	0.95	7.60	40.80	0.80	0.05

Table 5.6: Baseline final cooling cell hardware in terms of cell geometry, solenoid fields and absorber geometry

Cell no.	RF freq. MHz	Num. RF	Tot. RF len. cm	Max. RF grad. MV/m	Rot RF phase deg	Initial KE MeV	Final KE MeV	Energy spread MeV	Bunch len. mm
1	0.0	0	0	0	0	73.8	39.4	4.4	141
2	111.1	10	2.5	19.81	-180	53.7	32.7	2.8	241
3	56.9	17	4.25	14.17	90	53.0	32.5	4.1	406
4	40.1	17	4.25	11.9	51	49.0	31.4	3.9	348
5	34.9	9	2.25	11.11	-10	35.6	16.9	5.7	781
6	30.6	15	3.75	10.4	-54	28.3	14.7	2.7	1256
7	11.6	19	4.75	6.823	-82	32.6	13.3	3.1	1319
8	16.2	9	2.25	8.04	67	21.4	14.0	3.2	1692
9	13.4	13	3.25	7.32	67	24.1	12.4	3.5	1962
10	8.2	13	3.25	5.39	-6	16.5	8.8	2.8	2702
11	5.7	15	3.75	4.48	-96	16.3	11.2	2.9	3013

Table 5.7: Short rectilinear final cooling cell RF parameters. 0^o phase is on-crest mode.

5.3 Final cooling (long rectilinear)

A high-field final cooling system has also been designed that would follow the end of rectilinear B-10. This system is more demanding in terms of magnet parameters (exceeding present development target) but yields good performance. The parameters are listed in Tables 5.8, 5.9, 5.10 and 5.11.

The Final cooling (high-field) lattice described below is stored in the `Final_cooling_updated` repo as release `2024-10-03-prerelease`

Stage	ε_T mm	ε_L mm	ε_{6D} mm^3	Cumulative transmission %
Start	0.14	1.5	0.030	100
Stage 1	0.12	2.0	0.030	99.60
Stage 2	0.099	3.8	0.038	96.60
Stage 3	0.082	5.0	0.034	87.80
Stage 4	0.060	7.1	0.026	81.60
Stage 5	0.046	9.7	0.022	72.20
Stage 6	0.034	17.9	0.021	63.90
Stage 7	0.024	35.3	0.022	60

Table 5.8: Long rectilinear final cooling cell performance parameters

Stage	Stage length (m)	Peak on-axis Bz (T)	LH absorber length (m)
Stage 1	1.564	38.5	0.203
Stage 2	2.735	-45.2	0.188
Stage 3	2.984	28	0.0736
Stage 4	2.949	-43.4	0.0547
Stage 5	2.781	46.2	0.064
Stage 6	5.6	-40.7	0.0575
Stage 7	5.494	50	0.0654

Table 5.9: Long rectilinear final cooling cell magnet lattice parameters

Stage	Frequency MHz	Number of RF cells	Maximum gradient MV/m	Phase °	RF cell length m
stage 1		0			
stage 2	133.09	3	15	14.26	0.25
stage 3	109.84	2	11.1	44.94	0.25
stage 4	69.6	3	5.64	12.24	0.25
stage 5	54	5	7.4	41.97	0.25
stage 6	23.6	9	5.5	21.3	0.25
stage 7	11.2	9	5.25	46.56	0.25

Table 5.10: Long rectilinear final cooling cell RF parameters. 0^o phase is bunching mode.

Stage Units	Final Pz MeV/c	Final energy spread MeV	Final $c\sigma_t$ c
Start	95	3.35	0.04794
Stage 1	77.1	4.218	0.07809
Stage 2	56.7	2.546	0.19776
Stage 3	53.9	2.117	0.3408
Stage 4	42.1	1.983	0.4467
Stage 5	42.68	2.681	0.3999
Stage 6	37.03	2.811	0.8124
Stage 7	36.42	2.694	1.4994

Table 5.11: Long rectilinear inal cooling cell beam longitudinal parameters

5.4 Pre-accelerator

No pre-accelerator design exists. Table 5.12 gives estimations of design and performance based on induction LINAC technology.

Injection Energy MeV	Extraction Energy MeV	Pulse Length ns	Transmission %	Linac Length m
5	250	15	86	140

Table 5.12: Pre-Accelerator (Induction Linac) - see for example RADLAC-1

6 Low Energy Acceleration

The low energy acceleration chain brings the muon beams from $250\,\mathrm{MeV}$ after the pre-accelerator to $63\,\mathrm{GeV}$ for injection into the high energy acceleration chain described in Section 7.

It is composed of a single-pass superconducting LINAC outlined in Table 6.1, followed by two recirculating linear accelerators (RLA), described in Table 6.2.

RLA2 has an preliminary optics design. No optics design exists for LINAC and RLA1. Both RLAs have an assumed racetrack geometry. The transmission through RLA2 is 92.6%. The target transmission for LINAC and RLA1 is 90%, which corresponds to an effective average gradient of $4.1\,\mathrm{MV/m}$.

	CryoModule 1	CryoModule 2
Initial energy [GeV]	0.255	–
Final energy [GeV]	–	1.25
Frequency [MHz]	325	325
RF gradient [MV/m]	20	20
Passes	1	1

Table 6.1: Parameters describing the single-pass LINAC that follows the final cooling section.

	RLA1		RLA2	
Initial energy [GeV]	1.25		5	
Final energy [GeV]	5		63	
Energy gain per pass	0.85		13.5	
Frequency [MHz]	352	1056	352	1056
No. SRF cavities	36	4	600	80
RF length [m]	61.2	3.4	1020	68
RF gradient [MV/m]	15	25	15	25
Passes	4.5		4.5	
Linac length [m]	–		915	
Arc lengths [m]	–		≈ 300	

Table 6.2: Multi-pass recirculating LINACs

7 High Energy Acceleration

As described in [13], an option for the chain of four rapid cycling synchrotrons (RCS) foresees to accelerate two counter-rotating bunches at a repetition rate of 5 Hz in stages of 0.30 TeV (RCS1), 0.75 TeV (RCS2) and 1.5 TeV (RCS3) to inject into the 3 TeV collider ring, or 5 TeV (RCS4), to inject to the 10 TeV collider ring. This scenario is based on the US Muon Acceleration Program (MAP) [14, 2] and applied for a general Greenfield site. The high-energy stage of the accelerator chain with four RCS is illustrated in Fig. 7.1. Corresponding site-specific parameter designs can be found in Section 16.

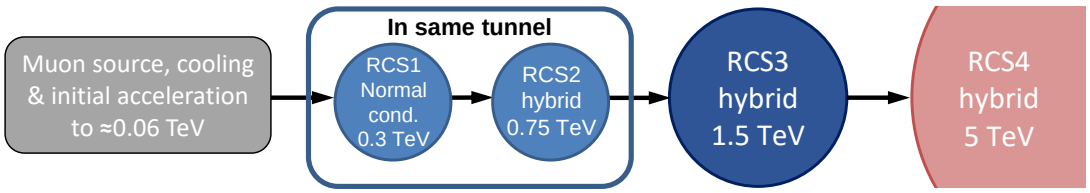

Fig. 7.1: Schematic of the chain of rapid cycling-synchrotrons for the high-energy acceleration complex. From [13].

The first two RCS share the same tunnel, meaning that they have the same circumference and layout [15]. The bending in the first RCS is provided by normal conducting magnets. The RCS2 to RCS4 are planned as hybrid RCSs where normal conducting magnets cycling from $-B_{\mathrm{nc}}$ to $+B_{\mathrm{nc}}$ are interleaved with strong fixed-field, superconducting magnets. Within this section, NC magnets are referred to as *pulsed*, and the SC magnets are referred to as *steady*. This is to reflect the alternative magnet technologies required for the hybrid RCS. This combination allows for a large energy swing with a high average bending field to minimize the travel distance of the muons and thus their decay losses. The absolute value of magnetic field in the normal-conducting dipoles does not exceed $\pm 1.8\,\mathrm{T}$ at injection and extraction for all RCSs to avoid saturation of the magnet yoke. For the hybrid RCS2 and RCS3, the magnetic field in the SC magnets is $10\,\mathrm{T}$ to provide a compromise between the magnet filling factor and magnet costs. To protect the SC magnets from decay products, the inner aperture of the SC magnets is larger with $10\,\mathrm{T}$. Increasing the field to $16\,\mathrm{T}$ implies higher technological and financial cost without a significant improvement of the machine performance. In the case of RCS4 however, the average magnetic field in the accelerator is assumed to be $16\,\mathrm{T}$ as a higher magnetic field in the SC magnets helps to reduce the overall circumference and thus the muon decay and RF requirements. This requirement may evolve with the optimization of the high-energy chain.

The number of synchrotron oscillations per turn is extreme [13], much larger than the conventional stability limit for stable synchrotron oscillations and phase focusing of $1/\pi$ in a synchrotron with one or few localized RF sections. To mitigate resulting beam losses, the RF system must be distributed over the entire RCSs. Tracking simulations on how the number of RF stations influences the longitudinal emittance have been performed. For the present design, the minimum number is around 32 RF stations for RCS1 and RCS4, and 24 stations for RCS2 and RCS3 [13].

It is worth noting that the longitudinal dynamics used values of momentum compaction factor for an RCS lattice design based on FODO cells. With a more defined optics design, this number might change and with it the basic parameters of the longitudinal beam dynamics such as the synchrotron tune, bucket area and energy acceptance, which are all a function of the momentum compaction factor.

7.1 Parameter tables

Table 7.1 shows the general RCS parameters, and Table 7.2 specifies lattice parameters. The first parameters for the fourth RCS to accelerate to $5\,\mathrm{TeV}$ are included but may evolve in the near future. We assume a survival rate of 90 % per ring and linear ramping only considering losses due to muon decay, even though these values are subject to further adjustments to optimize the RF and magnet powering parameters with respect to total costing, ramp shape, bunch matching, and the overall transmission of the entire chain.

Parameter	Unit	RCS1	RCS2	RCS3	RCS4
Hybrid RCS	-	no	yes	yes	yes
Repetition rate	Hz	5	5	5	5
Circumference	m	5990	5990	10700	35000
Injection energy	GeV	63	314	750	1500
Extraction energy	GeV	314	750	1500	5000
Energy ratio		5.0	2.4	2.0	3.3
Assumed survival rate		0.9	0.9	0.9	0.9
Cumulative survival rate		0.9	0.81	0.729	0.6561
Acceleration time	ms	0.34	1.10	2.37	6.37
Revolution period	µs	20	20	36	117
Number of turns	-	17	55	66	55
Required energy gain/turn	GeV	14.8	7.9	11.4	63.6
Average accel. gradient	MV/m	2.44	1.33	1.06	1.83
Number of bunches		1	1	1	1
Inj. bunch population	10^{12}	2.7	2.4	2.2	2
Ext. bunch population	10^{12}	2.4	2.2	2	1.8
Beam current per bunch	mA	21.67	19.5	9.88	2.75
Beam power	MW	640	310	225	350
Vert. norm. emittance	µm	25	25	25	25
Horiz. norm. emittance	µm	25	25	25	25
Long. norm. emittance	eVs	0.025	0.025	0.025	0.025
Bunch length at injection	ps	31	30	23	13
Bunch length at ejection	ps	20	24	19	9
Straight section length	m	2335	2335	3977	10367
Length with pulsed dipole magnets	m	3654	2539	4366	20376
Length with steady dipole magnets	m	-	1115	2358	4257
Max. pulsed dipole field	T	1.8	1.8	1.8	1.8
Max. steady dipole field	T	-	10	10	16
Ramp rate	T/s	4200	3282	1519	565
Main RF frequency	GHz	1.3	1.3	1.3	1.3
Harmonic number		25900	25900	46300	151400

Table 7.1: RCS acceleration chain key parameters

Parameter	Unit	RCS1	RCS2	RCS3	RCS4
Fill ratio dipole	%	61	61	62.8	70.4
Cells per arc		5	4	6	9
Number of arcs		34	26	26	26
Cell length	m	30.1	53	64.3	133.6
Relative path length difference	10^{-6}	0	8.3	2	1.7
Vertical aperture	mm	40	33.0	28.2	29.6
Transition gamma		46.2	29.2	36.9	59.0
Momentum compaction factor	10^{-4}	4.68	11.74	7.35	2.87

Table 7.2: RCS acceleration chain lattice parameters

8 Collider

The present work concentrates on the design of a 10 TeV center-of-mass collider. The aim is to maximize the luminosity to the two possible experiments. The basic assumptions are extrapolations from lower energy starting with a relative rms momentum spread of $\sigma_\delta = 1 \cdot 10^{-3}$. Together with the longitudinal emittance, this fixes the rms bunch length $\sigma_z = 1.5$ mm and the $\beta^* = 1.5$ mm to the same value, such that the hour glass luminosity reduction factor $f_{hg} = 0.758$ starts to become significant. Maximization of the luminosity requires to choose the shortest possible circumference C compatible with feasibility of the magnets (average bending field assumed to be $\bar{B} \approx 10.48$ T leading to $C \approx 10$ km). Note that extrapolation of parameters to higher energies lead to very large chromatic effects further increasing with energy.

The main parameters are described in Table 8.1, which contains a set of target parameters which meet the performance of Table 2.1. The set of relaxed parameters considers a lattice with reduced beta oscillations and chromatic aberrations, to study imperfections and the effects of movers.

The radial build of arc dipoles is described in Table 8.2. The radial build assumes a radiation shielding thickness of 3 cm, which can be accepted from a cryogenics point of view if the operating temperature is 20 K. The estimated heat load and radiation damage in arc dipoles is summarized in Table 14.3.

		version	
Parameter	Unit	relaxed	target
Center of mass energy	TeV	10	
Geometric Luminosity[1]	$10^{34}\,\mathrm{cm}^{-2}\,\mathrm{s}^{-1}$	5.77	19.2
Beam energy	TeV	5	
Relativistic Lorentz factor		47322	
Circumference	km	≈ 10	
Dist. of last magnet to IP	m	6	
Repetition rate	Hz	5	
Bunch intensity (one bunch per beam)	10^{12}	1.80	
Injected beam power per beam	MW	7.2	
Normalized transverse rms emittance	µm	25	
Longitudinal norm. rms emittance	eVs	0.025	
Relative rms momentum spread	10^{-3}	0.3	1
RMS bunch length in space	mm	5	1.5
RMS bunch length in time domain	ns	.017	0.005
Twiss betatron function at the IP	mm	5	1.5
Energy loss per turn[2]	MeV	≈ 27.2	
Integrated RF gradient[3]	MV	30	

Table 8.1: 10 TeV collider main parameters

[1] Luminosities for Gaussian beams with hour glass reduction factor and without beam-beam effect. Multiturn beam simulations with the correct lattice and tunes are needed in addition to first single pass simulations resulting in a modest luminosity increase.

[2] Assuming constant bending field of 15 T. The exact value will depend on the detailed lattice design and likely be lower.

[3] Assuming that only the synchrotron radiation losses have to be compensated. Some margin and no particular frequency requirements as long as the RF voltage does not vary too much over the bunch length of few 10s of ns.

Parameter	Unit	Thickness	Outer radius
Beam aperture	mm	23.49	23.49
Coating (copper)	mm	0.01	23.5
Radiation absorber (tungsten alloy)	mm	30	53.5
Shielding support and thermal insulation	mm	11	64.5
Cold bore	mm	3	67.5
Insulation (Kapton)	mm	0.5	68
Clearance to coils	mm	1	69

Table 8.2: Collider arcs, coil inner aperture. For options using low temperature superconductor, i.e. at 3 TeV, the shielding thickness should be 40 mm and the other parameters changed accordingly.

9 Machine-Detector Interface

The beam-induced background arising from muon decay poses a significant challenge for the physics performance of a multi-TeV muon collider. The machine-detector interface relies on massive absorbers in close proximity to the interaction point (IP) to reduce the number of secondary particles reaching the detector. This section describes the geometrical features of the shielding and quantifies the flux of secondary background particles. In addition, the ionizing dose and displacement damage in different parts of the detector are presented.

9.1 Nozzle geometry and material composition

The innermost part of the machine-detector interface consists of a nozzle-like shielding, which defines the inner detector envelope. The nozzle extends from the last magnet ($L^* = 6$ m) to almost the IP and must be made of a high-Z and high density material to shield efficiently the electromagnetic showers induced by the decay electrons and positrons. All studies carried out so far were based on the slightly modified nozzle geometry than the one developed within the Muon Accelerator Program (MAP) [16, 17]. Although the MAP nozzle was optimized for a center-of-mass energy of 1.5 TeV, it has been used as a starting point for the first 10 TeV studies (see, for example, Refs. [18, 19]).

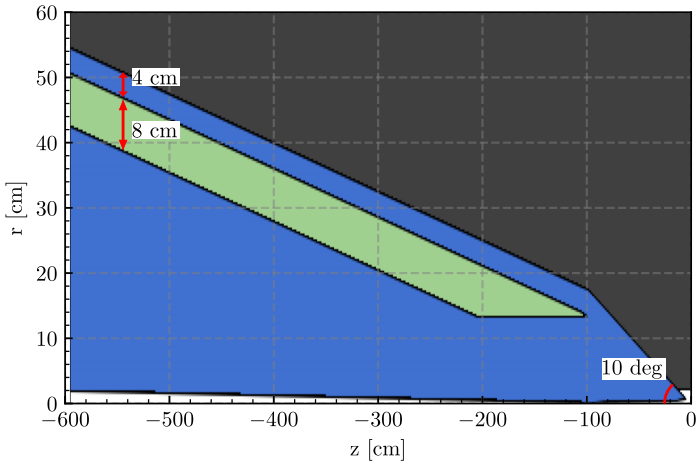

Fig. 9.1: Left nozzle geometry dimensions. The blue layer is made of INERMET180 (registered trademark), a heavy tungsten alloy, while the green one is composed of borated polyethylene.

Figure 9.1 illustrates the modified MAP nozzle geometry in the $z - r$ plane, where z is the beam axis and r is the radial coordinate. The nozzle is assumed to have azimuthal symmetry around the z-axis. The figure shows only the nozzle on the left side of the IP; the second nozzle has the same shape but is mirrored with respect to the interaction point. The nozzle is assumed to consist mainly of INERMET180 (registered trademark), a tungsten-based alloy (blue color), with a layer of borated polyethylene on the outer surface (green color) to thermalize and absorb neutrons before they reach the detector. Using a tungsten alloy (instead of pure tungsten) is required to allow the manufacture of such shielding elements, however such a choice reduces slightly the shielding effectiveness of the nozzle due to the lower material density. The beam pipe connecting the two opposite nozzles is made of beryllium, with an internal radius of 2.3 cm and a thickness of 1 mm.

The nozzle tip is located at a distance of 6 cm from the IP. The inner aperture of the nozzle features three

z [cm]	r [cm]
Outer surface of nozzle	
595	55
100	17.57
6	1
Outer surface of the borated polyethylene layer	
595	51
100	13.57
Inner surface of the borated polyethylene layer	
595	43
204.49	13.47
100	13.47
Inner aperture of the nozzle	
595	1.78
100	0.3
15	0.6
6	1

Table 9.1: Nozzle Dimensions

different angles, with an aperture bottleneck at $100\,\mathrm{cm}$ from the IP. In the region between $100\,\mathrm{cm}$ and the first magnet at $600\,\mathrm{cm}$, the inner nozzle surface increases and is defined by the required beam clearance to avoid direct halo losses on the aperture. The outer surface of the nozzle follows a conical shape, with two different angles. Near the interaction point, the inclination amounts to 10 degrees, which determines the angular acceptance of the detector. All the space outside the nozzle and the central beam pipe can be occupied by the detector. The present setup is of conceptual nature, without yet considering engineering aspects or a possible support structure for the nozzle.

Table 9.1 summarizes the coordinates of the inner aperture and outer surface of the nozzle, respectively. Table 9.2 provides the material components of the nozzle.

Component	Density [g/cm3]	Element	Atomic Fraction (mass fraction if negative)
EM Shower Absorber	18	W	-0.95
		Ni	-0.035
		Cu	-0.015
Neutron Absorber	0.918	H	0.5
		C	0.25
		B	0.25

Table 9.2: Material composition of nozzle

9.2 Beam-induced background

The number of background particles entering the detector per bunch crossing depends on the nozzle geometry, the nozzle material composition and the interaction region layout. Table 9.3 summarizes the number of secondary electrons, positrons, photons and neutrons reaching the detector in a 10 TeV muon collider. The numbers were obtained with FLUKA Monte Carlo simulations, considering the nozzle introduced in the previous section. The bunch intensity was assumed to be 1.8×10^{12} muons. Only secondary particles with energies above a given threshold value were considered (see Table 9.4).

Table 9.3: Number of secondary particles (muon decay) entering the detector volume (10 TeV). Only particles above the threshold values in Table 9.4 were included. The multiplicities include only the contribution of one beam and correspond to one bunch crossing.

Particle type	**Particles entering detector**
Photons	1.0×10^8
Neutrons	1.1×10^8
Electron/positrons	1.2×10^6
Muons	1.1×10^4
Charged hadrons	4.0×10^4

Table 9.4: Particle production and transport thresholds assumed in the background simulations.

Particle type	**Threshold**
Electrons, positrons and photons	100 keV
Hadrons and muons	100 keV
Neutrons	0.01 meV

The number of background particles presented in this section includes only the contribution from muon decay, which is expected to be the dominant source of beam-induced background. Other background sources can include muon halo losses on the aperture and incoherent electron-positron pair production.

9.3 Ionizing dose and displacement damage in detector

To evaluate the cumulative radiation damage in detector equipment, two quantities have been considered: the total ionizing dose and the 1 MeV neutron-equivalent fluence in Silicon. The former is a measure for the radiation damage in organic materials and compounds, while the latter is related to the displacement damage. The studies assumed a CLIC-like detector and the nozzle described above. The results for the vertex detector, the inner tracker, as well as the electromagnetic calorimeter are presented in Table 9.5 and correspond to one year of operation, assuming 1.2×10^7 seconds of operation (139 days). The studies considered only muon decay, while neglecting the contribution of collision products and beam halo losses. The results were computed for IR lattice version 0.8.

Table 9.5: Maximum values of the ionizing dose and the 1 MeV neutron-equivalent fluence (Si) in a CLIC-like detector. All values are per year of operation (10 TeV) and include only the contribution of muon decay.

	Radius	Dose	1 MeV fluence (Si)
Unit	cm	kGy	10^{14} n/cm^2
Vertex detector	3	1000	10
Inner tracker	12	70	15
ECAL	150	2	2

10 Detectors

The design of the detector for $\sqrt{s} = 10$ TeV follows the concept already developed for $\sqrt{s} = 3$ TeV with modifications to account for the higher energy. Two distinct detector concepts are presented, MAIA (Muon Accelerator Instrumented Apparatus) and MUSIC (MUon System for Interesting Collisions), to fully exploit the two interaction points of the collider. Both designs share a similar structure, a cylinder 11.4 m long with a diameter of 12.8 m. The main detector components are:

- Tracking system
- Electromagnetic calorimeter (ECAL)
- Hadron calorimeter (HCAL)
- A superconducting solenoid
- A muon sub-detector

The origin of the space coordinates is the beam interaction point. The z-axis has direction parallel to the beam pipe, the y-axis is parallel to gravity acceleration and the x-axis is defined as perpendicular to the y and z axes.

Table 10.1 summarises the detector parameters sub-system by sub-system for the two concepts. While the tracking system has a similar structure, the MAIA detector has the solenoid just after the tracker, before the ECAL while MUSIC places the solenoid magnet between ECAL and HCAL.

Detector **MAIA / MUSIC**	**R_min** mm	**R_max** mm	**|Z|_min** mm	**|Z|_max** mm	**Ang. Acc.** °	**X / X0**	**L / L0**
Inner Trackers	30 / 28	1500	0	2300	10 – 170	0.1 to 0.3	0.04 to 0.1
EM Cal							
Barrel	1857 / 1690	2124 / 1960	0	2307 / 2210	10 – 170	42 / 38	1.9 / 1.7
Endcap	310	2124 / 1960	2307	2577		40 / 33	1.8 / 1.4
HAD Cal							
Barrel	2125 / 2902	4112 / 4756	0	2575 / 2609	10 – 170	100 / 89	10.9 / 9.5
Endcap	307	4112 / 4756	2575	4562 / 4434		114 / 116	12.3 / 12.5
Muon Systems							
Barrel	4150 / 4806	7150 / 6800	0	4565 / 4444	10 – 170	–	–
Endcap	446	7150 / 6800	4565 / 4444	6025 / 5903		–	–
Solenoid	1500 / 2055	1857 / 2862	–	2307 / 2509	–	6 / 18	1.4 / 2.7
Nozzle	10	55	–	5950	0.2 – 10	–	–

Table 10.1: Detector parameters for MAIA and MUSIC concepts. Values that are left empty ("–") are not relevant for the specific detector. X/X0 and L/L0 are for a particle traveling from the IP.

10.1 Tracking System

The tracking detector is composed of the vertex and tracker sub-detectors, both of them structured in barrels and end-caps. The barrels are cylindrical surfaces with variable lengths and radii, whose axes coincide with the beam pipe and cover the central part of the detector. The endcaps are annuli centered on the z axis, with variable distance from the interaction point and radii which cover the forward part of the detector. The major characteristics of this sub-system are described in Table 10.2.

The vertex detector is close to the interaction point in order to allow a good resolution on track impact parameter. The building blocks of the barrel detection layers are rectangular staves of sensors, arranged to form a cylinder, while the endcaps are constituted by trapezoidal modules of sensors, arranged as

"petals" to form a disk. The MAIA detector has 5 layers, with the first two structured as a double layer, while MUSIC has 5 distinct layers. The length of the MUSIC barrel is 26 cm, which is double that of MAIA.

The barrel layers have silicon pixels of size 25×25 μm^2, and thickness 50 μm. The eight endcaps layers, four for each side of the interaction point are composed of silicon pixels of size 25×25 μm^2 and thickness 50 μm and 16 modules.

The inner and outer trackers are based on the same technology for MAIA and MUSIC, single layer of silicon sensors of 100 μm thickness.

Strips on the barrels are oriented with the long side parallel to the beam axis while the end-caps are composed of radial modules composed by rectangular pads.

Sub-Detector MAIA/MUSIC Units	**Technology**	**# Layers /Rings**	**"Cell" Size** μm^2	**Sensor Thickness** μm	**Hit Time Resolution** ps	**Signal Time Window** ns	**Max Dose** kGy	**Max Fluence 1 MeV (Si)** 10^{14} n cm^{-2}
Vertex Barrel	Pixels	4*/5	25 x 25	50	30	[-0.18, 15.0]	1000	10
Vertex Endcap	Pixels	4	25 x 25	50	30	[-0.18, 15.0]	1000	10
Inner Barrel	Macro-Pixels	3	50 x 1000	100	60	[-0.36, 15.0]	70	15
Inner Endcap	Macro-Pixels	7	50 x 1000	100	60	[-0.36, 15.0]	70	15
Outer Barrel	Macro-Pixels	3	50 x 10000	100	60	[-0.36, 15.0]	< 70	–
Outer Endcap	Macro-Pixels	4	50 x 10000	100	60	[-0.36, 15.0]	< 70	–

Table 10.2: Specifications for MAIA and MUSIC Tracker Sub-Detectors. * The first layer is a double-layer with a 2mm gap.

10.2 Calorimeter System

The calorimeter system is composed of the electromagnetic and hadron sub-detectors. A summary of the main characteristics are in Table 10.3.

Sub-Detector MAIA / MUSIC Units	**Technology**	**Cell Size** mm^2	**# Longitudinal Slices**	**Time Resolution** ps	**Integration Time** ns	**Signal Time Window** ns	**Max Dose** kGy	**Max Fluence 1 MeV (Si)** 10^{14} n cm^{-2}
EM Cal - Barrel	W+Si / Crystal	5 x 5	50 / 6	/50	/25	[-0.25, 10]	2	2
EM Cal - Endcap	W+Si / Crystal	5 x 5	50 / 6	/50	/25	[-0.25, 10]	2	2
HAD Cal - Barrel	Iron + Scint.	30 x 30	75 / 70	–	–	[-0.25, 10]	–	–
HAD Cal - Endcap	Iron + Scint.	30 x 30	75 / 70	–	–	[-0.25, 10]	–	–

Table 10.3: Electromagnetic and Hadronic Calorimeters parameters for MAIA and MUSIC.

The MAIA ECAL configuration is inspired by CLIC. It consists of a dodecagonal barrel and two endcap systems. It is composed of 40 interlaced layer of Tungsten as absorber material 2.2 mm thick and Si sensor as active material with 5×5 mm^2 silicon detector cells. It is located outside of the superconducting solenoid.

The MUSIC ECAL, has the same shape of MAIA, but is positioned immediately after the tracking system and within the superconducting solenoid. It is a semi-homogeneous calorimeter based on Lead Fluoride (PbF_2) crystals read out by surface mounted ultraviolet extended Silicon Photomultipliers. It represents a modern design approach that aims to combine the intrinsic high-energy resolution of homogeneous calorimeters with the longitudinal segmentation typically found in sampling calorimeters.

MAIA and MUSIC currently share the same technology for HCAL. It consists of a dodecagonal barrel and two endcap systems, structured in 60 interlaced layers of iron absorber 20 mm thick and plastic

scintillating tiles with cell size 30×30 mm^2. It allows the reconstruction of hadronic jets and helps in particle identification, to separate hadrons from leptons and photons.

The characteristics of the superconducting solenoid are reported in table 10.4

B [T]	Thickness [mm]	max |z| [m]	Bore Radius [m]
5	356 / 393	2307 / 2509	1680 / 2459

Table 10.4: Magnetic field of both detector concepts, thickness of the coil for MUSIC, and dimensions.

10.3 Muon System

The current configuration of the two detector concepts does not include a magnetic field outside the calorimetric system, so the role of the muon detector must be reconsidered. In particular, for high-energy muons, new methods based on machine learning, which combine tracking detector and calorimeter information, could be employed. In this case, the muon detector would primarily serve to identify that the particle is a muon.

11 Magnets

Here we provide a summary of the magnet parameters for the study so far.

11.1 Magnet Needs and Challenges

The short muon lifetime (2.2 µs at rest) and production of bright muon beams results in a unique set of demands for magnet technologies, including large-bore high-field solenoids, dipoles and quadrupoles, compact ultra-high-field solenoids, and very fast-ramping dipoles. Activities within the scope of the IMCC has led to the most advanced set of main magnet conceptual designs and performance parameters. These parameters are an evolution of previous studies, in particular the U.S. Muon Accelerator Program (MAP) [20], extending the performance space by considering recent advances in magnet technology.

First an overview of the magnet options is provided, then four key sub-sections of the accelerator complex are addressed, with corresponding demands in terms of magnet performance.

1. Front-end: Target solenoids in Section 11.3.
2. Cooling: HTS 6D solenoids and high-T final cooling solenoids in Section 11.4.
3. Acceleration: Rapid-cycling and hybrid-cycling dipoles in Section 11.5.
4. Collider: Dipoles in Section 11.6.

11.2 Magnet Studies and Technology Options

The main performance targets and target ranges (i.e., not yet to specification) of the most challenging magnets of the muon collider are shown Table 11.1. Though these targets are bound to adapt as the study proceeds, they already provide a good basis to feedback on beam optics and accelerator performance, and to identify outstanding issues to be addressed by future work and dedicated R&D. The whole accelerator complex functions in steady state, apart from the fast ramped magnets in the rapid cycling synchrotrons.

Complex Unit	Magnet	No.	Aper. [mm]	Length [m]	Field [T]	Grad. [T/m]	Ramp rate [T/s]	Temp. [K]
Target, capture	Solenoid Coils	23	1380	≈ 0.4 – 0.8	2 – 20		SS	20
6D cooling	Solenoid Coils	≈ 6000	90-1500	0.08 – 0.5	2 – 17		SS	4.2-20
Final cooling	Solenoid Coils	14	50	0.5	>40		SS	4.2
RCS	NC dipole	≈ 1500	30x100	5	± 1.8		4200	300
	SC dipole	≈ 2500	30x100	1.5	10		SS	4.2-20
Collider arc	Dipoles	≈ 1050	140	5	14*		SS	
	CF	≈ 628	140	5 – 10	4 – 8	±100–±150*	SS	4.2-20
IR	quadrupoles	≈ 20	100 - 280	5 – 10		±110 – ±330**	SS	4.2-20

Table 11.1: Summary of main magnet development targets. For the collider magnet values marked with a * slightly higher values are assumed in the lattice design but no important changes are expected adjusting to the specified performances. The values marked with ** correspond to the lattice design but might be too high for the magnets; the lattice design will be updated accordingly. Specific configurations still need to be evaluated and this is a work in progress. CF stands for combined-function magnets.

11.3 Front End (muon production and capture)

The details for the current target and front-end parameters are shown in Section 4.1 and 4.2.
The target for muon production is inserted in a steady-state, high field solenoid which has outer dimension in the range of 150 to 250 mm, depending on technology. It captures the pions and guides them

into a decay and capture channel, also embedded in solenoid magnets. To maximize capture efficiency, the magnetic field profile along the axis of the channel needs to have a specific shape, with peak field of $20\,\mathrm{T}$ on the target, and an adiabatic decay to approximately $1.5\,\mathrm{T}$ at the exit of the channel, over a total length of approximately $18\,\mathrm{m}$.

Besides the high field values, another challenge derives from the radiation environment due to the interaction of the multi-MW proton beam with the target. The radiation requirements for this system are explained further in Section 14. A large bore dimension implies high stored magnetic energy, which in turn affects electromagnetic forces, magnet protection, and cost as we will discuss later.

11.3.1 Target solenoid

Following recent advances in HTS magnets for fusion [21] [22] we have proposed a configuration based on an HTS cable operated at $20\,\mathrm{K}$ [23] [24]. The analysis performed so far shows that it is possible to eliminate the resistive insert and reduce the magnet bore to $1380\,\mathrm{mm}$, almost half of that of the US-MAP LTS coil, still producing the desired field profile for muon capture efficiency. Operation at temperature higher than liquid helium reduces the need to shield the radiation heat, maintaining good overall energy efficiency. The proposed system has a stored energy of $\approx 1\,\mathrm{GJ}$, a coil mass of $\approx 100\,\mathrm{t}$ and wall-plug power consumption of $\approx 1\,\mathrm{MW}$, i.e. a considerable reduction with respect to the hybrid solution proposed earlier.

11.4 Cooling

The overview of the cooling system parameters are in Section 5, which factors in our evolving understanding of acceptable solenoid parameter limits. We are presently performing analysis and optimization on this latest configuration.

To the first order, the final emittance of the muon beam is inversely proportional to the strength of the final cooling solenoids. The design study from MAP was based on a $30\,\mathrm{T}$ final cooling solenoid, and demonstrated that an emittance roughly a factor of two greater than the transverse emittance goal can be achieved [25]. Other studies [26] show that fields in the range of $50\,\mathrm{T}$ improve the final emittance requirements and offer further gains in beam brightness. To improve upon these results, we are considering an HTS final cooling solenoid with the potential to reach an excess of $40\,\mathrm{T}$.

11.4.1 6D Cooling solenoids

In the current configuration, a total of 3054 solenoids are spread over a 0.85 km distance. There are 14 unique cell types, and 26 unique solenoid types. During the beam dynamics studies, we integrated a magnet design guide to constrain allowable magnet geometries and current densities based on key solenoid parameters (stresses σ, stored magnetic energy e_m, critical current density J_c). To assess limits on these properties, we use HTS (ReBCO) from Fujikura FESC-SCH tape as a reference [28]. The parameters and limits implemented (considering a single solenoid) are: hoop stress, $\sigma_\theta < 300$ MPa; radial tensile stress, $\sigma_r < 20$ MPa; and stored magnetic energy density, $e_m < 150$ MJ/m^3. Additionally, we constrained the current density to not exceed the critical current density based on a large dataset of J_c measurements [29], taking HTS operating at 20 K with 2.5 K margin. We report in Tab. 11.2 main parameters of each cooling cell type and unique solenoid type.

Cell	E_{Mag} (MJ)	e_{Mag} (MJ/m^3)	Coil	$\boldsymbol{J_E}$ (A/mm^2)	B_{peak} (T)	σ_{Hoop} (Max.) (MPa)	σ_{Radial} (Min.) (MPa)	σ_{Radial} (Max.) (MPa)
A1	5.4	21	A1-1	57.6	5.2	42	-8	0
A2	22.1	106.1	A2-1	149.5	11.6	194	-48	0
A3	5.0	49.5	A3-1	131.5	10.1	121	-25	0
A4	8.0	92.3	A4-1	193.2	13.8	225	-51	1
B1	9.1	49.8	B1-1	96.9	7.7	104	-24	0
B2	15.6	64.2	B2-1	102.1	9.2	131	-32	0
B3	36.9	105.9	B3-1	127.9	12.9	208	-57	0
B4	75.6	149.9	B4-1	88.5	16.1	260	-1	29
B5	17.3	88.9	B5-1	179.6	14.7	295	-2	17
B5			B5-2	154.0	14.7	212	-57	1
B6	8.3	96.6	B6-1	214.4	15.3	339	-5	18
B6			B6-2	211.5	12.0	214	-6	6
B6			B6-3	212.7	12.4	162	-46	0
B7	8.2	87.7	B7-1	183.3	14.7	264	0	25
B7			B7-2	153.9	11.1	175	-4	10
B7			B7-3	210.3	13.2	180	-45	1
B8	8.8	92.1	B8-1	193.7	16.5	270	-6	38
B8			B8-2	202.1	15.4	270	-6	29
B8			B8-3	212.8	13.2	187	-50	0
B9	7.5	76.5	B9-1	256.4	17.2	281	0	37
B9			B9-2	88.4	10.0	95	-2	12
B9			B9-3	204.9	13.2	184	-46	0
B10	5.0	68.6	B10-1	326.8	19.2	378	0	49
B10			B10-2	146.1	11.1	105	-4	13
B10			B10-3	207.8	12.5	158	-43	1

Table 11.2: Table of various parameters for 14 cell types and 26 unique solenoid types in the latest 6D cooling optics [27]. Values correspond to solenoids operating in their respective cells within a lattice. Note that if the solenoid is operating stand-alone or in a single cell, some parameters take on higher or lower values.

Observing Tab. 11.2, we find some solenoids exceed allowed design limits, primarily in terms of large hoop stresses (B6-1, B10-1) and tensile radial stresses (B4-1, B7-1, B8-1, B8-2, B9-1, B10-1). The most problematic solenoid is B10-1, with a hoop stress of 378 MPa, tensile radial stress of 49 MPa, and peak field on the coil of 19.2 T which corresponds to it exceeding its J_c by 114%. Importantly though, most of the solenoids are within or near the allowed design limits demonstrating the success of the iteration of design parameters with beam optics to produce an initial set of solenoids.

11.4.2 Final Cooling solenoid

A total of 17 final cooling cells were part of the scheme devised by US-MAP to achieve minimum beam emittance, with bore field up to $30\,\mathrm{T}$. To improve upon the results obtained by US-MAP we are considering for the final cooling a solenoid design with the potential to reach and exceed $40\,\mathrm{T}$, a clear bore of $50\,\mathrm{mm}$, a magnet length of $500\,\mathrm{mm}$, and sufficiently compact in size as required for an accelerator magnet (considerations of mass, footprint, and cost) [30]. The operating current density

targeted is high, $650\,\mathrm{A/mm^2}$, to reduce the coil size, as well as the forces and stored energy. The coil size is exceptionally small, with a $90\,\mathrm{mm}$ outer radius.

The mechanics of the final cooling solenoid is designed to achieve a maximum hoop stress of $650\,\mathrm{MPa}$ and no tensile stress in any condition experienced by the coil. To this aim, the wound and soldered pancakes are loaded in radial direction by a stiff external ring that introduces a radial pre-compression of $200\,\mathrm{MPa}$, at room temperature. The radial pre-compression is chosen to nearly balance the outward electro-magnetic stress at $40\,\mathrm{T}$.

For the transverse resistance, our goal is to achieve quench protection through a low transverse resistance (possibly with means to actively trigger quench), while at the same time allowing full ramp in less than 6 hours, as well as field stability at flat-top better than 10 ppm/s.

11.5 Acceleration

An overview of the high-energy accelerator parameters is in Section 7. In the present baseline, the NC dipoles in the first RCS need to sweep from 0.36 to $1.8\,\mathrm{T}$ within $0.35\,\mathrm{ms}$ (i.e. a rate of $4\,\mathrm{kT/s}$). In the last HCS the NC dipoles swing from $-1.8\,\mathrm{T}$ to $1.8\,\mathrm{T}$, in $6.37\,\mathrm{ms}$ (i.e. a rate of about $560\,\mathrm{T/s}$).

Design concepts of NC fast ramped magnets were developed by US-MAP, for peak operating field of $1.5\,\mathrm{T}$ [31]. SC dipoles for HCS were not yet studied in detail, besides setting target values for bore field and magnet length. Beyond magnet engineering, the primary challenge of an accelerator ring of the required dimension is that the stored energy is of the order of several tens of MJ. Powering at a high-pulse rate with good energy recovery efficiency between pulses will require mastery in the management of peak power in the range of tens of GW. Resonant circuits combined with energy storage systems seem to be the only viable solution. A high energy storage density and high quality factor are mandatory to limit foot-print, energy consumption, capital and operating cost.

11.5.1 Synchrotrons (RCS and HCS) dipoles

A lower bound for the stored energy is the magnetic energy in the beam aperture, a nominal 30 mm (gap) x 100 mm (width). To limit saturation, affecting losses and field quality, we have taken an upper design field limit of 1.8 T for the resistive magnets. This corresponds to a magnetic energy of 3.9 kJ/m in the beam aperture, while the energy stored in the magnet will be forcibly higher. The analysis of several resistive magnet configurations, of different iron cross section and materials, coil design and current density, shows that the lowest magnet stored energy is in the range of 5.4 kJ/m, a factor 1.4 higher than the magnetic energy in the beam aperture, quoted above [32]. A second issue is the magnitude of the resistive, eddy current and hysteresis loss. This is the power drawn from the grid, and dissipated. A suitable target, though not yet settled, is in the range of 500 J/m per pulse. Among all configurations analyzed, we have found that the best compromise of stored energy, loss and field quality is obtained with a “H” and “Hourglass” shaped iron core [32]. These configurations will be retained for further magnetic analysis, including 3D and end effects.

Finally, the design of the steady state superconducting magnets of the HCS’s is in development. Rejecting the cos-theta coil geometry due to its inefficiency for a rectangular aperture, our conceptual design focuses on flat racetrack coils which appear feasible to achieve a target field of around 10 T. With HTS, this could operate at temperatures significantly above liquid helium (10 to 20 K), offering gains in ef-

ficiency. We are currently progressing with detailed magnetic and mechanical simulations of potential configurations which can satisfy the field quality requirements while minimizing cost and engineering complexity.

11.6 Collider

An overview of the collider parameters is in Section 8, including the radiation shielding required for the head load due to muon decay. To allow for a compact collider ring and maintain sufficient space for shielding, the ring and Interaction Region (IR) dipole and quadrupole magnets thus need to be high-field and large aperture.

It is assumed that the main arc magnets have combined functions (e.g. dipole/quadrupole and dipole/sextupole) and generate a steady-state magnetic field up to $16\,\mathrm{T}$ in a $160\,\mathrm{mm}$ aperture. The most recent optics requires dipole fields in the range of $10\,\mathrm{T}$ and gradients of $300\,\mathrm{T/m}$. These field demands, combined with the aperture constraints, are presently only an initial evaluation, but they exceed practical limits of what is possible, and will require iteration. For the IR quadrupole magnets the assumption from the optics studies is of a peak field of $20\,\mathrm{T}$, also associated with large apertures, up to $200\,\mathrm{mm}$.

11.6.1 Collider dipoles

Using analytical evaluations of operating margin, peak stress, hot-spot temperature, and magnet cost under the assumption of a sector coil geometry [33] we have produced design charts of maximum magnet aperture (A) vs. bore field (B), which is a form convenient for iterating with the beam optics. Such A-B charts are shown in Figure 11.1 for a choice of superconductor and operating point of Nb3Sn at 4.5 K and ReBCO at 20 K.

For a 10 TeV collider, Nb-Ti at 1.9 K does not appear as a good solution because of low operating margin (recall the large energy deposition), as well as considerations of cryoplant efficiency and energy consumption. Similarly, Nb_3Sn at 4.5 K falls short of the required field performance for the arc magnets, being limited by peak stress and operating margin. It can provide feasible solutions only up to 14 T, which can be considered for a 3 TeV MuC ($\sim$ 11 T, 150 mm aperture). Our initial evaluation of ReBCO shows that also in this case the available design space does not match the required performance. For ReBCO, however, operating margin is not an issue, and operation in the range of 10 K to 20 K could be envisaged. The main limitations come rather from the cost of the superconductor, and from quench protection. Cost considerations drive the current density in an all-HTS coil towards high values, in the range of 800 to 1000 A/mm2, where standard detect-and-dump protection strategies are not sufficiently fast. It is hence clear that alternative protection schemes need to be devised to benefit from the large current carrying capacity and margin of present REBCO conductors. Provided that the cost per m of REBCO tape can be reduced by a factor three to four, relaxing the need for very high values of current density, we have found that a suitable design range for the arc magnets can be defined using two points, from a nominal aperture of 140 mm at reduced bore field of 14 T, up to nominal bore field of 16 T but reduced aperture of 100 mm. The whole range can be achieved with REBCO at 4.5 K and 20 K, while the low field range can be reached also with Nb3Sn at 4.5 K, thus providing at least two technology options.

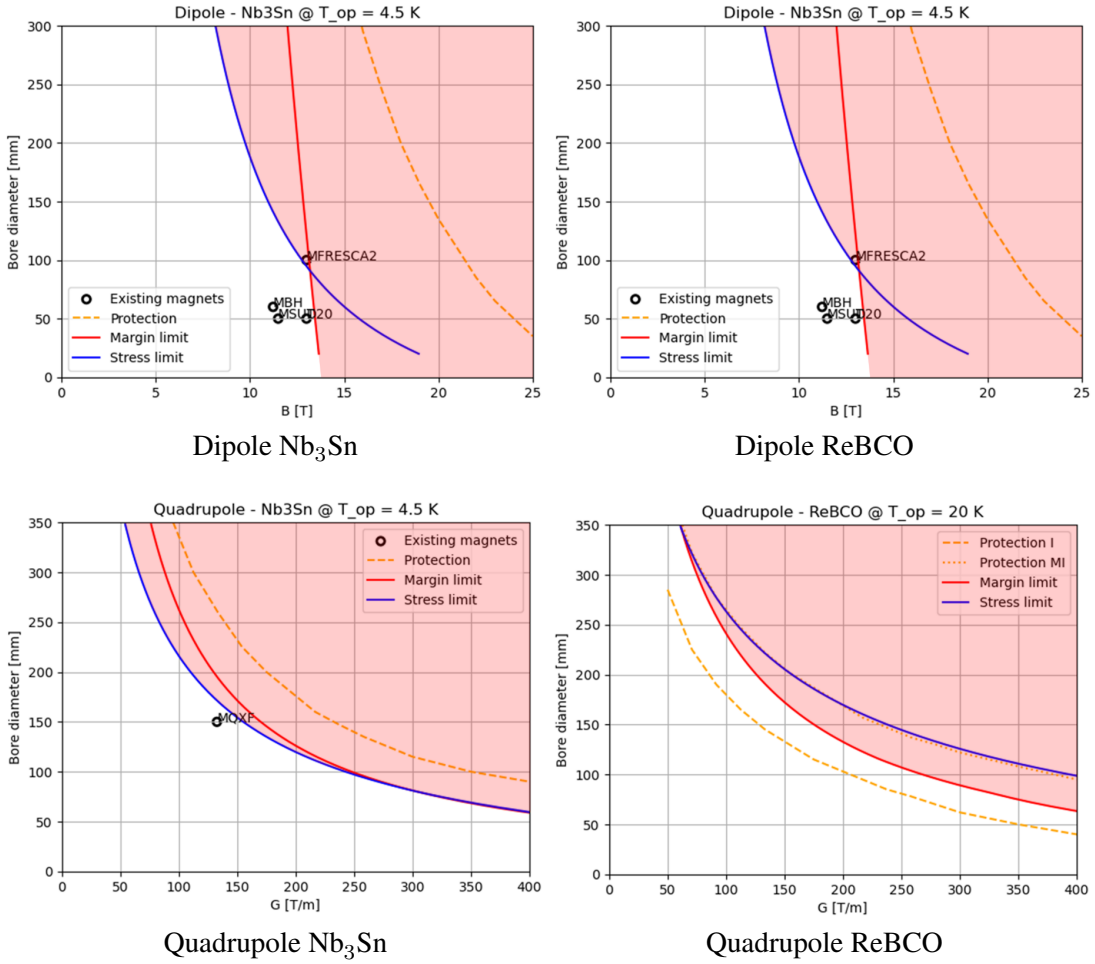

Dipole Nb_3Sn Dipole ReBCO

Quadrupole Nb_3Sn Quadrupole ReBCO

Fig. 11.1: A-B plots for dipole (top) and quadrupole (bottom) collider magnets made of either Nb_3Sn (left) at 4.5 K or ReBCO (right) at 20 K. For ReBCO, the white region is the allowed area, assuming the magnet is metal-insulated [34].

The semi-analytic tool [33] discussed in this section has been very successful to provide quick feedback and iteration with beam dynamics, energy deposition and cryogenics team during this design stage. Currently, this tool is being adapted to consider quadrupole performance limits (for the design of the interaction regions) and combined function magnets, as required because of neutrino flux mitigation. Upcoming work will focus on more detailed magnetic and mechanical designs of ARC dipoles and IR quadrupoles.

12 RF

The RF parameters which should be considered in the design are listed in Table 12.1.

Table 12.1: RF frequencies and gradients to be used in the beam dynamics studies.

Proton driver				
Linac				
RF frequencies	MHz	352	704	
Muon cooling complex				
6D-cooling channels				
RF frequencies	MHz	352	704	1056
Maximum accelerating field in cavity (conservative)	MV/m	22	30	30
Maximum accelerating field in cavity (optimistic)	MV/m	35	50	50
Acceleration complex				
Linacs				
RF frequencies	MHz	352	704	1056
Maximum accelerating field in cavity (conservative)	MV/m	20	25	30
Maximum accelerating field in cavity (optimistic)	MV/m	30	38	45
RCSs				
RF frequency	MHz		704	1056, 1300
Maximum accelerating field in cavity (conservative)	MV/m		25	30
Maximum accelerating field in cavity (optimistic)	MV/m		38	45

In the other sub-systems of the muon cooling complex: capture, bunch merge, final cooling, etc many different RF frequencies are necessary. It is recommended to keep these RF frequencies as high as reasonable possible from the beam dynamics point of view, since the size of the achievable gradient scales approximately as $\sqrt{(f_{RF})}$.

12.1 RF systems for rectilinear cooling

The preliminary RF cavity design for each stage of the rectilinear cooling channel was developed based on the shape presented in [35] following the beam dynamics specification in Table 5.4. The other geometrical parameters characterizing the cavity shape are chosen to maximize the shunt impedance ($R/Q \cdot Q_0$) and reduce surface losses (P_{diss}) on the windows and cavity walls. The peak surface electric field (E_{peak}) is also minimized to avoid RF breakdown risk. The RF cavity frequency (f_0), the cavity length (L_{cav}), and the nominal RF gradient along the cavity axis (E_{nom}) for the studied RF cavities are reported in Table 5.4. Table 12.2 summarizes the relevant RF figures of merit computed for the operating frequencies of the studied cavities. Most of the power is dissipated in the cavity walls.

The filling time t_{f}, which is the time required to fill the cavity to the nominal voltage $V_{\text{nom}} = E_{\text{nom}} L_{\text{cav}}$, is given by:

$$t_{\text{f}} \approx \frac{2Q_{\text{L}}}{\omega_0} \ln\left(\frac{2\beta_{\text{c}}}{\beta_{\text{c}} - 1}\right), \tag{12.1}$$

where $Q_{\text{L}} = Q_0/(1+\beta_{\text{c}})$, with Q_0 being the intrinsic quality factor, β_{c} the coupling factor, and ω_0 is the angular frequency of the cavity's operating mode. The beam duty factor (DF) can be calculated as

	Q_0	t_f	DF	R/Q	P_{diss}	$\frac{P_{\text{diss,Be}}}{P_{\text{diss}}}$	$E_{\text{peak,Cu}}$	$E_{\text{peak,Be}}$
	10^4	µs	10^{-4}	Ω	MW/cavity	-	MV/m	MV/m
Stage A1	3.06	31.203	1.17	171.73	4.25	0.377	11.72	27.383
Stage A2	3.14	32.087	1.21	149.68	4.34	0.085	23.249	26.511
Stage A3	2.20	11.248	0.43	160.36	2.06	0.201	20.802	31.507
Stage A4	2.22	11.345	0.43	150.21	2.21	0.085	27.873	31.829
Stage B1	3.91	39.954	1.51	183.70	2.78	0.23	12.392	21.651
Stage B2	3.56	36.323	1.37	170.47	3.24	0.164	16.376	23.361
Stage B3	3.15	32.148	1.21	141.27	4.07	0.031	26.175	24.429
Stage B4	3.59	36.71	1.38	154.02	3.92	0.009	27.732	22.823
Stage B5	2.23	11.366	0.43	140.85	1.18	0.026	24.116	22.027
Stage B6	2.22	11.36	0.43	137.40	2.34	0.007	37.092	29.544
Stage B7	2.22	11.354	0.43	136.87	2.11	3.08×10^{-3}	36.487	26.892
Stage B8	2.22	11.347	0.43	137.39	1.92	8.32×10^{-4}	35.95	23.73
Stage B9	2.22	11.344	0.43	138.11	2.14	3.16×10^{-4}	38.528	23.268
Stage B10	2.22	11.342	0.43	139.06	1.51	1.56×10^{-4}	32.522	18.341

Table 12.2: RF figures of merit for the RF cavities in the rectilinear cooling channel

the ratio between the average power and the peak dissipated power:

$$DF = \frac{P_{\text{ave}}}{P_{\text{diss}}} = \frac{\int_0^\infty P(t)\mathrm{d}t \cdot f_{\text{b}}}{V_{\text{acc}}^2/(R/Q \cdot Q_0)}, \tag{12.2}$$

where $P(t)$ is the time-dependent power calculated from the cavity voltage profile and $V_{\text{acc}} = TTF \cdot V_{\text{nom}}$ the accelerating cavity voltage, with TTF being the Transit-Time factor, given by:

$$TTF = \frac{\int_{z_{\min}}^{z_{\max}} E_z e^{jkz}\, dz}{\int_{z_{\min}}^{z_{\max}} E_z\, dz}, \tag{12.3}$$

where $k = \omega_0/(\beta c)$ is the wave number with c being the speed of light in a vacuum and β the relativistic velocity factor. The geometric shunt impedance, R/Q, is calculated, considering the TTF as:

$$\left(\frac{R}{Q}\right) = \frac{|V_z(0,0)|^2}{\omega_0 U_0} TTF^2, \tag{12.4}$$

where $U = \omega_0$ is the energy stored in the cavity.

Table 12.5 reports the power requirements for each stage of the cooling channel. The peak input RF power is given by:

$$P_{\text{g}} = P_{\text{diss}}\beta_{\text{c}}. \tag{12.5}$$

The duty factor of the RF power source (DF_{g}) is given as the ratio between the average power of the generator and the peak input RF power.

$$DF_{\text{g}} = \frac{P_{\text{ave,g}}}{P_{\text{g}}} = \frac{P_{\text{g}} t_{\text{f}} \cdot f_{\text{b}}}{P_{\text{g}}}, \tag{12.6}$$

The total plug power for the RF systems was calculated considering the generator (η_{G}) and modulator (η_{M}) efficiencies reported in Table 12.3 as:

$$P_{\mathrm{g,ave,tot}} = \frac{N_{\mathrm{cav}} P_{\mathrm{ave,g}}}{\eta_{\mathrm{G}} \eta_{\mathrm{M}}}, \tag{12.7}$$

where N_{cav} is the total number of cavities for each stage.

Parameters	Symbol	Unit	Value
Coupling factor	β_{c}	-	1.2
Bunch repetition frequency	f_{b}	Hz	5
Generator efficiency	η_{G}	-	0.7
Modulator efficiency	η_{M}	-	0.9

Table 12.3: RF parameters for the rectilinear cooling channel

For the RF frequency, cavity length and nominal RF gradient of the rectilinear cooling RF system, please refer to Table 5.4. Table 12.4 displays in addition the RF cavity window radius, window thickness and the relativistic beta of the muon beam at each stage.

	Window radius mm	Window thickness μm	Relativistic β -
Stage A1	240	120	0.923
Stage A2	160	70	0.894
Stage A3	100	45	0.894
Stage A4	80	40	0.901
Stage B1	210	100	0.882
Stage B2	190	80	0.879
Stage B3	125	50	0.882
Stage B4	95	45	0.889
Stage B5	60	30	0.889
Stage B6	45	20	0.888
Stage B7	37	20	0.887
Stage B8	27	20	0.884
Stage B9	23	10	0.881
Stage B10	21	10	0.884

Table 12.4: Beam dynamics specifications for the RF cavities in the rectilinear cooling channel

	P_g MW/cavity	DF_g 10^{-4}	N_{cav} -	$P_{g,tot}$ MW	$P_{g,av}$ kW	$P_{g,av,tot}$ kW
Stage A1	5.094	1.560	348	1772.7	277.09	439.83
Stage A2	5.21	1.610	356	1854.9	297.87	472.82
Stage A3	2.468	0.567	405	999.4	56.70	90.00
Stage A4	2.655	0.573	496	1317.1	75.41	119.70
Stage B1	3.336	2.001	144	480.4	96.11	152.56
Stage B2	3.883	1.819	170	660.1	120.09	190.61
Stage B3	4.882	1.611	216	1054.5	169.92	269.72
Stage B4	4.701	1.843	183	860.3	158.54	251.65
Stage B5	1.419	0.573	275	390.1	22.37	35.51
Stage B6	2.809	0.572	220	617.9	35.35	56.11
Stage B7	2.531	0.572	204	516.4	29.55	46.90
Stage B8	2.304	0.572	276	635.8	36.39	57.77
Stage B9	2.573	0.571	212	545.4	31.15	49.45
Stage B10	1.806	0.572	196	354.1	20.26	32.16

Table 12.5: RF power requirements in the rectilinear cooling channel

12.2 RF systems for low-energy acceleration

In the low-energy acceleration, only the design of RLA2 is being considered for the computation of RF parameters. The baseline cavity geometry is chosen to be the LEP2 cavity. A summary of the assumed parameters can be found in Table 12.6. For the calculation of the losses in the power generation, the parameters of the ILC-powering system were used (Table 12.8). The resulting powering parameters for the RLA2 cavities can be found in table 12.7.

Table 12.6: Parameters of the LEP2 cavity from [36]

Parameter	Symbol	Unit	Value linearizer	Value accelerator
Fundamental mode RF frequency	f_{RF}	MHz	352	1056
Accelerating gradient	G_{acc}	MV/m	15	25
Geometric shunt impedance	R/Q	[Ω]	247.25	360.72
Active length	l_{active}	m	1.686	0.845
Total length	l_{total}	m	1.851	1.011
Number of cells	-	-	4	6
$E_{\text{peak}}/E_{\text{acc}}$	-	-	2.4	2.4
$B_{\text{peak}}/E_{\text{acc}}$	-	mT/(MV/m)	3.9	3.9
Iris aperture (inner/end cell)	-	mm	286/241	94/80
Cavity quality factor	Q_0	-	$\geq 1 \times 10^{10}$	$\geq 1 \times 10^{10}$
Cell-to-cell coupling	k_{cc}	%	1.51	1.62

Parameter	Unit	RLA2 acc	RLA2 lin
Synchronous phase	°	95	275
Frequency	MHz	352	1056
Number of bunches/species	-	1	
Combined beam current (μ^+, μ^-)	mA	134	
Total RF voltage	GV	15.2	1.69
Total number of cavities	-	600	80
Total number of cryomodules	-	200	16
Total RF section length	m	1110.6	80.8
External Q-factor	10^6	0.38	0.21
Cavity detuning for beam loading comp.	kHz	0.04	0.21
Beam acceleration time	µs	35.5	
Cavity filling time	µs	344	65
RF pulse length	ms	0.38	0.1
RF duty factor	%	0.19	0.05
Peak cavity power	kW	3425	2965
Average RF power	MW	5.16	0.16

Table 12.7: RF parameters for the low-energy acceleration chain. For the synchronous phase, 90° is defined as being on-crest

Table 12.8: ILC RF-power parameters [37] in the Distributed Klystron Scheme (DKS)

Parameter	Unit	Value
Max. klystron power	MW	10
Klystron efficiency	%	65
Wall plug RF power efficiency	%	∼48
Klystron repetition rate	Hz	5
Klystron frequency	MHz	1300
RF pulse length	ms	1.65
RF duty factor	%	0.83

12.3 RF systems for high-energy acceleration

A first approximation of the power requirements for the RCS chain has been performed using the ILC cavities, cryomodules, and powering infrastructures [37] as a baseline, the results of which can be found in Table 12.9.

The parameters of the ILC cavity can be found in Table 12.10. To calculate the losses, parameters from the ILC DKS powering scheme are used (Table 12.8). While these parameters are used for initial beam dynamics and power requirements studies, other frequencies and cavities are under investigation for muon acceleration. The requirements do not consider HOM power contributions, cryogenic losses and the impact of the detuning, which is necessary due to the orbit change during the acceleration. The calculated parameters assume a linear ramp of the magnet system. In the accelerator, a harmonic magnet ramp is foreseen, which will require additional cavities.

The change in the cavity detuning and external quality factor stems from the inclusion of transient beam loading effects in the calculation of the powering parameters. As a result, the power consumption of the system also changes.

		RCS1	RCS2	RCS3	RCS4	All
Synchronous phase	°	135	135	135	135	-
Number of bunches/species	-	1	1	1	1	-
Combined beam current (μ^+, μ^-)	mA	43.3	39	19.8	5.49	-
Total RF voltage	GV	20.9	11.2	16.1	90	138.2
Total number of cavities	-	683	366	524	2933	4506
Total number of cryomodules	-	76	41	59	326	502
Total RF section length	m	962	519	746	4125	6351
Combined peak beam power (μ^+, μ^-)	MW	640	310	225	350	-
External Q-factor	10^6	0.696	0.775	1.533	5.522	-
Cavity detuning for beam loading comp.	kHz	-1.32	-1.186	-0.6	-0.166	-
Beam acceleration time	ms	0.34	1.1	2.37	6.37	-
Cavity filling time	ms	0.171	0.19	0.375	1.352	-
RF pulse length	ms	0.51	1.29	2.73	7.77	-
RF duty factor	%	0.19	0.57	1.22	3.36	-
Peak cavity power	kW	1128	1017	516	144	-
Total peak RF power	MW	1020	496	365	561	-
Total number of klystrons	-	114	53	38	57	262
Cavities per klystron	-	6	7	14	52	-
Average RF power	MW	1.919	2.84	4.43	18.92	28.1
Average wall plug power for RF system	MW	2.95	4.38	6.811	29.1	43.25
HOM power losses per cavity per bunch	kW	25.85	26.16	16.24	5.75	-
Average HOM power per cavity	W	366	384	287	86	-

Table 12.9: RF parameters for the RCS chain. The average RF power includes losses from the cavity to the klystron, while the wall plug power also includes the klystron efficiency. For the synchronous phase, 90° is defined as being on-crest

Table 12.10: Parameters of the TESLA cavity from [37] and [38]

Parameter	Symbol	Unit	Value
Fundamental mode RF frequency	f_{RF}	MHz	1300
Accelerating gradient	G_{acc}	MV/m	30
Geometric shunt impedance	R/Q	Ω	518
Geometry factor	G	Ω	271
Active length	l_{active}	m	1.065
Total length	l_{total}	m	1.247
Number of cells	-	-	9
$E_{\text{peak}}/E_{\text{acc}}$	-	-	2.0
$B_{\text{peak}}/E_{\text{acc}}$	-	mT/(MV/m)	4.26
Iris aperture (inner/end cell)	-	mm	70/78
Cavity quality factor	Q_0	-	$\geq 1 \times 10^{10}$
Longitudinal loss factor ($\sigma_z = 1mm$)	$k_{\|\|}$	V/pC	11.05
Cell-to-cell coupling	k_{cc}	[%]	1.87

13 Impedance

This section is devoted to beam intensity limitations that could be encountered in the different machines due to collective effects.

13.1 Impedance model for the Rapid Cycling Synchrotrons

Impedance models for the four RCS of the acceleration chain were developed. The Rapid Cycling Synchrotrons (RCS) will be comprised of many RF cavities to provide the large acceleration voltage needed to reach the muon survival target, as developed in Section 7. It is assumed that the RCS 1, 2, 3 and 4 have respectively 700, 380, 540 and 3000 cavities. Because of their number, the cavities are expected to be a large contributor to the RCS impedance model. The models assume that superconducting TESLA cavities [39] are used for the RF system, and include the High-Order Modes (HOMs) generated by these cavities [40]. The HOMs parameters for a single cavity are reported in Table 13.1.

Frequency f_{res}	$\frac{R_s}{Q}$	Q factor	Shunt impedance R_s
GHz	[kΩ/m]	$[1 \times 10^4]$	[MΩ/m]
1.659	0.10	31.4	32.61
1.705	1.05	1.35	14.16
1.706	1.21	1.34	16.27
1.728	0.97	0.0413	0.4
1.729	0.45	0.0381	0.17
1.736	1.25	0.0516	0.64
1.737	0.95	0.0574	0.54
1.761	0.35	0.583	2.04
1.762	0.28	0.621	1.72
1.788	0.16	0.867	1.43
1.789	0.18	0.890	1.61
1.798	0.11	1.23	1.29
1.799	0.10	1.21	1.27
1.865	0.79	3.91	30.87
1.865	0.83	4.12	34.07
1.874	1.09	3.88	42.32
1.874	1.07	4.39	47.14
1.88	0.22	4.23	9.38
1.88	0.24	5.15	12.21
2.561	0.13	0.0620	0.08
2.561	0.12	0.0527	0.07
2.577	2.05	0.364	7.46

Table 13.1: HOMs from TESLA cavity, complete table, for a single cavity.

An alternate type of cavity, the Low Losses [41] type based on the TESLA one, was considered in previous studies and the HOMs of this cavity are reported in Table 13.2.

Frequency f_{res} GHz	$\frac{R_s}{Q}$ [kΩ/m]	Q factor [1×10^4]	Shunt impedance R_s [MΩ/m]
1.717	0.70	4.0	27.8
1.738	0.41	6.0	24.7
1.882	0.43	0.6	2.6
1.912	0.57	0.9	5.2
1.927	1.93	1.5	29
1.94	1.49	2.0	29.8
2.451	3.08	10	307.8
2.457	2.16	5.0	107.9
3.057	0.04	30	11.7
3.06	0.03	80	25

Table 13.2: HOMs from Low Loss TESLA cavity, complete table, for a single cavity.

However the HOMs of the Low Losses cavities generate stronger wakefields and are more detrimental to beam stability [42]. The RCS parameters relevant for the impedance and coherent stability simulations are reported in Table 13.3.

Parameter	Unit	All RCS rings	
		Horizontal	Vertical
Average Twiss beta	m	50	50
Chromaticity Q'	-	+20	+20
Detuning from octupoles	m^{-1}	0	0
Transverse damper	turns	20	
Bunch intensity at injection	muons/bunch	2.7×10^{12}	

Table 13.3: RCS Collective Effects Parameters used in simulations.

A second important contributor to the impedance model of the RCS is the normal conducting magnets vacuum chamber. Because of the high ramping rate, a large eddy current would appear if a fully metallic chamber was used [43]. A ceramic chamber with a thin metallic coating on the inner surface would therefore be used [44]. Its dimension and characteristics are reported in Table 13.4.

Parameter	Unit	Value
Inner dimension width, height	mm, mm	30, 20
Titanium coating thickness	μm	1 to 10
Ceramic thickness	mm	5
Outer dimension width, height	mm, mm	40, 30

Table 13.4: RCS 2 normal conducting magnets vacuum chamber used in simulations.

Transverse coherent stability simulations were performed to evaluate the impact of the RF cavities and vacuum chambers. To mitigate the instabilities, a transverse damper system can be used to damp the transverse centroid motion of the bunches, and/or chromaticity can be introduced with sextupoles. Parametric scans were performed to find if those are needed and, if necessary, the chromaticity Q' required. The chromaticity was scanned from $Q' = -20$ to $Q' = +20$, and the transverse damper from a 4-turn to a 100-turn damping time, with an additional case without damper.

Tracking simulations were performed using Xsuite [45] and PyHEADTAIL [46]. The bunch motion is

simulated through the complete RCS chain. Muon decay is not included in these simulations, therefore the bunch intensity remains constant through the chain, equal to the intensity of 2.7×10^{12} muons per bunch at injection in RCS 1. Results showed that a positive chromaticity of $Q' = +20$ is needed in the accelerators to stabilize the beams and leave enough margin for some initial transverse offset of the bunches, and a 20-turn transverse damper also helps stabilize the beams [47, 42].

13.2 Impedance model for the 10 TeV collider ring

In the $10\,\mathrm{TeV}$ collider ring, the main impedance source would be the resistive-wall contribution from the magnets' vacuum chamber. To protect the superconducting magnet coils from muon decay induced heating and radiation damage, a tungsten shield is proposed to be the inserted in the magnet cold bore as detailed in Section 14 and described in Ref. [48].

Previous parametric studies performed with Xsuite and PyHEADTAIL showed that a minimum chamber radius of $13\,\mathrm{mm}$, together with a copper coating on the inner diameter are required to ensure coherent transverse beam stability. The current dipole magnet radial build detailed in Section 11.6 foresees a $23.5\,\mathrm{mm}$ inner radius, with a $10\,\mu\mathrm{m}$ copper coating. The vacuum chamber properties used for the impedance model computation are summarized in Table 13.5.

Parameter	Unit	Value
Chamber geometry		circular
Chamber length	m	10000
Copper coating thickness	μm	10
Copper resistivity at 300 K	nΩ m	17.9
Tungsten resistivity at 300 K	nΩ m	54.4
Chamber radius (from magnet radial build)	mm	23
Min. chamber radius required (50-turn damper)	mm	13

Table 13.5: $10\,\mathrm{TeV}$ collider parameters for impedance model simulations.

A particularity of the collider ring is its isochronous operation (i.e. with $\eta \approx 0$) [49], obtained with the flexible momentum compaction cells described in Section 8. This is to avoid the large RF voltage that would be needed to bunch beams with very short length and large energy spread. However this freezes the synchrotron motion of the particles within the bunch and can lead to beam breakup instabilities such as those encountered in Linacs [50].

Transverse coherent beam stability simulations were performed with Xsuite and PyHEADTAIL, including the effect of muon beam decay [51]. The beam parameters used for these simulations are summarized in Table 13.6. With a chromaticity of $Q' = 0$, the beam becomes unstable over its lifetime in the collider, leading to large transverse emittance growth [51]. A slightly positive chromaticity of $Q' = +2$ is needed to introduce a betatron frequency spread that helps stabilize the beam.

Parameter	Unit	Value
Circumference	m	10 000
Beam energy	TeV	5
Bunch intensity at injection	muons/bunch	1.80×10^{12}
1σ bunch length	mm	1.5
Longitudinal emittance $\epsilon_l = \sigma_z \sigma_E$	$\mathrm{MeV\,m}$	7.5
Transverse normalized emittance	$\mu\mathrm{m\,rad}$	25
Momentum compaction factor		0
Total RF voltage	MV	0

Table 13.6: $10\,\mathrm{TeV}$ collider machine and beam parameters.

14 Radiation

This Section presents radiation studies for the following systems:

- Target solenoids considering proton impact on a Graphite target in Section 14.1.
- Magnets in the arcs and interaction regions of the collider ring due to muon decay in Section 14.2.
- Neutrino-induced dose in soil for mono-directional muons in Section 14.3.

The latter can serve as dose kernel for computing surface dose levels under consideration of the beam optics and the collider placement.

14.1 Radiation load on the target superconducting solenoids

Generic radiation load studies for the superconducting solenoid were performed by means of FLUKA Monte Carlo simulations. A 5 GeV proton beam with a beam sigma of 5 mm and a beam power of 2 MW was assumed to impinge on a graphite target rod (see Table 4.5 for the target dimensions). The target was centered along the beam axis and therefore no dependence on the azimuthal angle can be expected. The simulation results for the coils are presented in Table 14.1, showing the maximum displacement per atom (DPA) per year and the maximum yearly absorbed dose. The studies were carried out for different target shielding thicknesses and shielding compositions. The shielding inner radius in the area of the target vessel is fixed at $17.8\,\mathrm{cm}$. The gap between the shielding outer radius and the magnet coils is always kept at $7.5\,\mathrm{cm}$. The shielding outer radius can be read from the table by subtracting $7.5\,\mathrm{cm}$ from the magnet coils' inner radius. The target shielding was either assumed to be made of pure tungsten or tungsten with an outer, neutron-absorbing layer made of water combined with boron-carbide.

The maximum DPA per year in the magnet coils is reduced by a factor of 1.8 with every $5\,\mathrm{cm}$ of extra tungsten. Exchanging $2.5\,\mathrm{cm}$ of tungsten for a layer of $2\,\mathrm{cm}$ of water followed by $0.5\,\mathrm{cm}$ of boron-carbide enclosed by an external layer of $1\,\mathrm{cm}$ of tungsten is equivalent to thickening pure tungsten shielding by $5\,\mathrm{cm}$ in the context of reducing the yearly DPA in the magnet coils. In this way, the DPA can be decreased without the necessity of increasing the total shielding radius. In the presence of the external layer of tungsten enclosing the water-boron-carbide layer, the absorbed dose is not affected by the reduction in the total thickness of tungsten. Previous studies have shown that if the tungsten was not placed after the special neutron-absorbing layer, the absorbed dose in the magnets would increase, most likely due to the photon production in the neutron capture of hydrogen (sharp line at $2.2\,\mathrm{MeV}$). Moreover, it was found that the reduction of the DPA per year thanks to the presence of water saturates

Table 14.1: Radiation load on the target superconducting magnet coils in terms of the maximum displacement per atom (DPA) and the maximum absorbed dose per year of operation for various shielding configurations.

	Tungsten + Water + Boron-Carbide		
Inner radius of the magnet coils	Shielding thickness around the target	DPA/year [10^{-3}]	Dose [MGy/year]
60 cm	**(B)W** 31.2 cm **+ H_2O** 2 cm **+ B_4C** 0.5 cm **+ W** 1 cm	1.70 ± 0.02	10.0 ± 0.3
65 cm	W 36.2 cm + H_2O 2 cm + B_4C 0.5 cm + W 1 cm	0.90 ± 0.02	5.6 ± 0.2
70 cm	W 41.2 cm + H_2O 2 cm + B_4C 0.5 cm + W 1 cm	0.49 ± 0.01	3.1 ± 0.1
75 cm	W 46.2 cm + H_2O 2 cm + B_4C 0.5 cm + W 1 cm	0.29 ± 0.01	1.9 ± 0.1
80 cm	W 51.2 cm + H_2O 2 cm + B_4C 0.5 cm + W 1 cm	0.16 ± 0.01	1.0 ± 0.1
85 cm	W 56.2 cm + H_2O 2 cm + B_4C 0.5 cm + W 1 cm	0.09 ± 0.01	0.6 ± 0.1

for a 3 cm-thick water layer. Therefore, only the results for one water-boron-carbide layer configuration is presented in Table 14.1.

14.2 Muon decay in the collider ring

The radiation-induced power load and radiation effects in collider equipment are dominated by the products of muon decay. While decay neutrinos yield a negligible contribution to the radiation load on the machine, the decay electrons and positrons induce secondary particle showers, which dissipate their energy in the surrounding materials. A continuous shielding is therefore needed, which dissipates the induced heat and protects the superconducting magnets against long-term radiation damage. Shielding studies for muon colliders have been previously carried out within MAP [52, 53, 54]. In particular, the shielding must:

- prevent magnet quenches,
- reduce the thermal load to the cryogenic system (by reducing the heat load to the cold mass of magnets),
- prevent magnet failures due to the ionizing dose in organic materials (e.g. insulation, spacers) and atomic displacements in the superconductor.

The assumed beam parameters and operational scenarios for the radiation studies are summarized in Table 14.2. The beam parameters (10 TeV) originate from Table 8.1, but are repeated here for completeness.

Table 14.2: Parameters for radiation studies (collider ring). The number of decays consider the contribution of both beams.

	Units	3 TeV	10 TeV
Particle energy	TeV	1.5	5
Bunches/beam		1	1
Muons per bunch	10^{12}	2.2	1.8
Circumference	km	4.5	10
Muon decay rate per unit length	$10^9\,\mathrm{m}^{-1}\,\mathrm{s}^{-1}$	4.9	1.8
Power ($e^{\pm}$)/meter	kW/m	0.411	0.505
Operational years	years	5-10	
Operational time per year (average)	days	139	

The power carried by decay electrons and positrons is on average 35 % of the energy of decaying muons. With the presently assumed beam parameters, this amounts to about 500 W/m. The remaining 65 % of the energy released in decays is carried away by neutrinos. Assuming five years of operation and an average operational time of 1.2×10^7 s/year, the total number of decays in the collider ring reaches almost $3 \times 10^{17}\,\mathrm{m}^{-1}$ for the 3 TeV collider, and about $1 \times 10^{17}\,\mathrm{m}^{-1}$ for the 10 TeV collider. In an alternative scenario, the collider might operate for ten years, which means that that the number of decays increases by a factor of two. The results presented in the following subsections are given for one year of operation and need to be scaled to the actual operational scenario (5 or 10 years).

14.2.1 Power deposition, dose and DPA in arc magnets

In order to estimate the required shielding thickness for a 10 TeV collider, generic shielding studies for the arc magnets were performed with FLUKA [55, 56]. The studies considered only muon decay, whereas other source terms (e.g. beam halo losses) still have to be addressed in the future. Table 14.3 summarizes the calculated power load and radiation damage in collider ring magnets as a function of the radial absorber thickness (10 TeV collider). For simplicity, the FLUKA simulation model consisted of a generic string of 16 T dipoles, each six meters long; the drift regions between dipoles were assumed to be 20 cm long. As absorber material, we used tungsten due to its high atomic number and density (tungsten was also considered as shielding material by the MAP collaboration). For engineering reasons, pure tungsten may be substituted by tungsten-based alloys without significantly affecting the shielding efficiency if the alloy has a similar material density. As beam aperture, we considered 23.5 mm like in the 1D radial build summarized in Table 8.1. A gap of 15.5 mm was assumed between the radiation absorber and inner coil aperture, which leaves space for the shielding support and thermal insulation (both not simulated), as well as cold bore and Kapton (both included in the simulation). As shielding thicknesses, we considered 2 cm, 3 cm and 4 cm. The second case (3 cm) corresponds to the radial build in Table 8.1.

As can be seen in Table 14.3, the power penetrating the tungsten absorber (mostly in the form of electromagnetic showers) amounts to 3.7% in the case of a 2 cm shielding, and decreases to 0.8% in the case of a 4 cm shielding. Most of this power is deposited in the cold bore and cold mass of the superconducting magnets. A small fraction of the power escapes from the magnets and is dissipated in the surrounding materials, in particular the tunnel wall and soil. These power estimates do not consider the power carried by the decay neutrinos as they are not relevant for the radiation load to the machine.

Table 14.3: Power load and radiation damage in collider ring arc magnets (10 TeV) as a function of the radial tungsten absorber thickness. The power penetrating the shielding does not include neutrinos, since they are not relevant for the radiation load to the machine; the percentage values are given with respect to the power carried by decay electrons and positrons. The results include the contribution of both counter-rotating beams.

	Unit	**2 cm**	**3 cm**	**4 cm**
Beam aperture	mm	23.5	23.5	23.5
Outer shielding radius	mm	43.5	53.5	63.5
Inner coil aperture	mm	59	69	79
Absolute power penetrating tungsten absorber	W/m	18.5	8	4
Fractional power penetrating tungsten absorber	%	3.7	1.6	0.8
Peak power density in coils	$\mathrm{mW/cm^3}$	6.3	2.1	0.7
Peak dose in Kapton insulation (1 year)	MGy	10.6	3.3	1.3
Peak dose in coils (1 year)	MGy	8.5	2.8	1
Peak DPA in coils (1 year)	10^5 DPA	1.5	1.2	1

For all considered shielding thicknesses, the power density in the coils remains below 10 $\mathrm{mW/cm^3}$, which is expected to be significantly less than the quench level of HTS or Nb3Sn-based magnets. The 5-year ionizing dose exceeds 50 MGy in the Kapton insulation in case of a 2 cm shielding, but is less than 20 MGy if the shielding thickness is 3 cm or more. This is compatible with typical dose limits of Kapton tapes (usually of the order of 30 MGy). Likewise, the cumulative DPA in the superconductor, which is

mainly induced by secondary neutrons, remains below critical values for any of the considered shielding thicknesses. In summary, the results show that the power leaking from the shielding and deposited in the cold mass is the most important factor for the shielding thickness. The studies presented in this section are representative for dipoles in the collider arcs, but a separate assessment for insertion region magnets is needed (see next section).

14.2.2 Dose in IR magnets

In the interaction region, which accommodates the final focus magnets and a chicane for background reduction, more radiation is expected to arrive on the machine elements. This is a consequence of the long straight section between the chicane and the chromaticity correction section, which leads to a build-up of decay products. As a consequence, the radial shielding thickness generally needs to be larger than in the arcs in order to remain below critical dose levels. Moreover, the beam size in this section is substantially larger than the one in the arc sections, therefore increasing the aperture requirements.

In Table 14.4, the different IR magnets and the corresponding ionizing dose is reported. Thicker shielding elements are required for the first three dipoles than for the final focus quadrupoles.

Table 14.4: Cumulative ionizing dose in final focus quadrupoles and chicane dipoles located in the insertion region (lattice version 0.8).

Name	L [m]	Shield thickness [cm]	Coil aperture [cm]	Peak TID [MGy/y]
IB2	6	6	16.0	1.3
IB1	10	6	16.0	3.1
IB3	6	6	16.0	4.9
IQF2	6	4	14.0	7.7
IQF2_1	6	4	13.3	4.6
IQD1	9	4	14.5	1.1
IQD1_1	9	4	14.5	3.7
IQF1B	2	4	10.2	6.4
IQF1A	3	4	8.6	3.6
IQF1	3	4	7.0	3.5

In case of 5 years of operation, the dose would remain below 40 MGy in all magnets, which is considered acceptable. However, the dose would become too high for 10 years of operation, exceeding even 70 MGy for one of the final focus quadrupoles (IQF2). Therefore, in case of an extended operational period, even more stringent requirements on the shielding would be required.

14.3 Neutrino radiation

The decay of muons in the collider ring produces very energetic neutrinos that have a non-negligible probability to interact far away from the collider in material near to the Earth's surface producing secondary particle showers. The goal is to ensure that this effect does not entail any noticeable addition to natural radiation and that the environmental impact of the muon collider is negligible, i.e. an effective dose of the order of 10 μSv/year, similar, for instance, to the impact from the LHC. For the environmental impact assessment, detailed studies of the expected neutrino and secondary-particle fluxes are being performed with FLUKA. The latter can be folded with the realistic neutrino source term taking into account the collider lattice to predict the effective dose and to design suitable methods for mitigation

and demonstration of compliance.

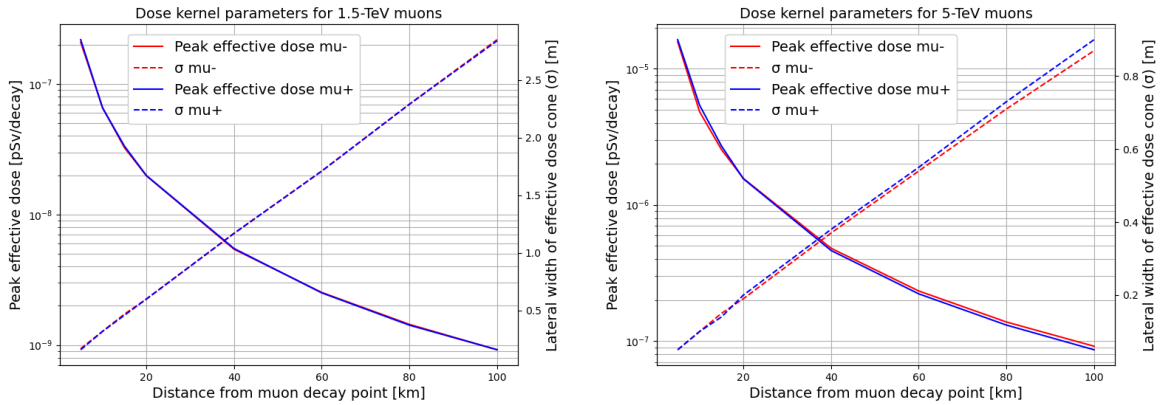

Fig. 14.1: Effective dose kernel parameters within soil as a function of the baseline distance from the muon decay point, for muon energies of 1.5 TeV (left) and 5 TeV (right).

FLUKA simulations were conducted to obtain the effective dose within soil resulting from the interaction of the neutrinos from the decay of 1.5 TeV and 5 TeV mono-directional muons. The angular distribution and the energy of the neutrinos were sampled taking into account the respective distributions from the muon decay. Moreover, the interactions were sampled such that the dose values corresponded to the values obtained when the neutrino-induced showers reach a plateau condition, i.e., after at least several meters of path through the material. The latter is a very conservative worst-case scenario as it does not consider that neutrino-induced showers rapidly decrease in the transition between soil and air.

The results of the FLUKA simulations are shown in Figure 14.1 in terms of dose kernel parameters, i.e., peak and lateral width of the effective dose profile at different baseline distances from the muon decay position. The values are reported in Tables 14.5 and 14.6 for the 1.5 TeV and 5 TeV muon beams.

Table 14.5: Effective dose kernel parameters of neutrino-induced radiation within soil at different baseline distances from the muon decay, for a muon beam energy of 1.5 TeV. The peak dose per muon decay and the lateral width of the dose profile (σ) have been derived from Gaussian fits of the FLUKA results.

	μ^-		μ^+	
Distance	**Peak eff. dose [pSv/decay]**	**σ [m]**	**Peak eff. dose [pSv/decay]**	**σ [m]**
5 km	$2.09 \cdot 10^{-7}$	0.17	$2.19 \cdot 10^{-7}$	0.16
10 km	$6.57 \cdot 10^{-8}$	0.32	$6.56 \cdot 10^{-8}$	0.32
15 km	$3.28 \cdot 10^{-8}$	0.47	$3.34 \cdot 10^{-8}$	0.46
20 km	$1.98 \cdot 10^{-8}$	0.60	$1.99 \cdot 10^{-8}$	0.60
40 km	$5.42 \cdot 10^{-9}$	1.17	$5.49 \cdot 10^{-9}$	1.17
60 km	$2.53 \cdot 10^{-9}$	1.71	$2.51 \cdot 10^{-9}$	1.71
80 km	$1.44 \cdot 10^{-9}$	2.29	$1.42 \cdot 10^{-9}$	2.29
100 km	$9.20 \cdot 10^{-10}$	2.85	$9.21 \cdot 10^{-10}$	2.84

These numbers shall be used as the basis for the calculation of the effective dose which takes into account realistic lattice parameters, i.e. factoring the associated distribution of muon trajectories in the sections of interest of the accelerator in, as well as the reduction due to realistic geometries and exposure scenarios. Additionally, mitigation methods, such as optimization of the source term, location

Table 14.6: Effective dose kernel parameters of neutrino-induced radiation within soil at different baseline distances from the muon decay, for a muon beam energy of 5 TeV. The peak dose per muon decay and the lateral width of the dose profile (σ) have been derived from Gaussian fits of the FLUKA results.

	μ^-		μ^+	
Distance	**Peak eff. dose [pSv/decay]**	**σ [m]**	**Peak eff. dose [pSv/decay]**	**σ [m]**
5 km	$1.57 \cdot 10^{-5}$	0.05	$1.63 \cdot 10^{-5}$	0.05
10 km	$4.86 \cdot 10^{-6}$	0.10	$5.38 \cdot 10^{-6}$	0.10
15 km	$2.54 \cdot 10^{-6}$	0.15	$2.70 \cdot 10^{-6}$	0.14
20 km	$1.56 \cdot 10^{-6}$	0.19	$1.55 \cdot 10^{-6}$	0.20
40 km	$4.80 \cdot 10^{-7}$	0.37	$4.62 \cdot 10^{-7}$	0.38
60 km	$2.33 \cdot 10^{-7}$	0.54	$2.22 \cdot 10^{-7}$	0.55
80 km	$1.38 \cdot 10^{-7}$	0.71	$1.31 \cdot 10^{-7}$	0.73
100 km	$9.16 \cdot 10^{-8}$	0.87	$8.63 \cdot 10^{-8}$	0.90

and orientation of the collider, should be considered.

The neutrino flux density arising from the collider ring arcs is expected to be reduced to a negligible level by deforming the muon beam trajectory, achieving a wide-enough angular spread of the neutrinos. Wobbling of the muon beam within the beam pipe would be sufficient for 1.5 TeV muon beam energy. At 5 TeV muon beam energy, the beam line components in the arcs may have to be placed on movers to deform the ring periodically in small steps such that the muon beam direction would change over time. Table 14.7 presents the effective dose within soil similar to Table 14.6, but taking into account the vertical deformation of the beam within ± 1 mrad by the movers. It results in a reduction factor of 80-90 of the saturated dose kernels within soil.

Table 14.7: Effective dose of neutrino-induced radiation within soil at different baseline distances from the muon decay after the vertical deformation by the movers is applied. The muon beam energy is 5 TeV. The reduction factor is the ratio between the peak dose value of the corresponding kernel from Table 14.6 and the dose value mitigated by the movers.

	μ^-		μ^+	
Distance	**Mitigated dose [pSv/decay]**	**Reduction factor**	**Mitigated dose**	**Reduction factor**
5 km	$1.97 \cdot 10^{-7}$	80	$2.04 \cdot 10^{-7}$	80
10 km	$6.09 \cdot 10^{-8}$	80	$6.74 \cdot 10^{-8}$	80
15 km	$3.18 \cdot 10^{-8}$	80	$3.15 \cdot 10^{-8}$	85
20 km	$1.86 \cdot 10^{-8}$	84	$1.94 \cdot 10^{-8}$	80
40 km	$5.56 \cdot 10^{-9}$	86	$5.50 \cdot 10^{-9}$	84
60 km	$2.63 \cdot 10^{-9}$	89	$2.55 \cdot 10^{-9}$	87
80 km	$1.53 \cdot 10^{-9}$	90	$1.50 \cdot 10^{-9}$	87
100 km	$9.99 \cdot 10^{-10}$	92	$9.73 \cdot 10^{-10}$	89

Instead of considering the saturated effective dose within soil, which is unrealistic for an annual exposure, various more realistic, yet conservative scenarios are under investigation, including exposure in building structures below and above the ground. The most conservative of these is illustrated in Figure 14.2, where two consecutive underground rooms are aligned along the neutrino flux path. Assuming a very conservative annual exposure scenario with a 100% occupancy in the two underground rooms would lead to a effective dose for various relevant distances as given in Table 14.8.

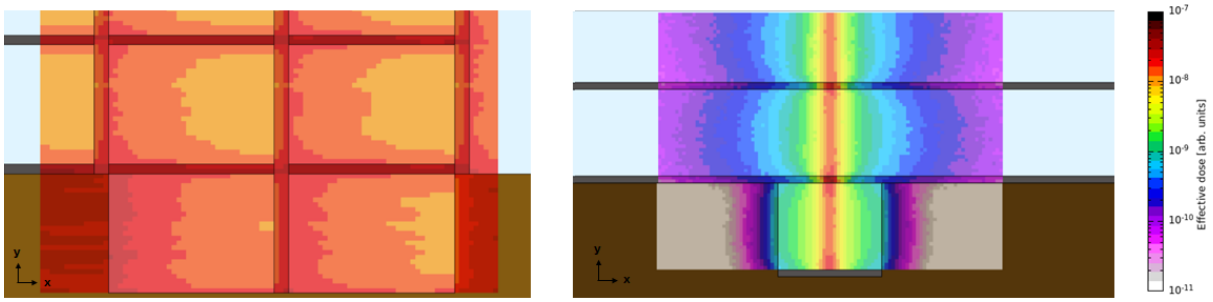

Fig. 14.2: Side (left) and cross-sectional view (right) of the effective dose (in arb. units) for an underground building structure exposed to the neutrino flux from the decay of negative muons after the vertical deformation by the movers.

Table 14.8: Effective dose of neutrino-induced radiation for an underground building structure at different baseline distances from the muon decay after the vertical deformation by the movers is applied. The muon beam energy is 5 TeV.

	μ^-	μ^+
Distance	**Mitigated dose [pSv/decay]**	**Mitigated dose[pSv/decay]**
15 km	$6.21 \cdot 10^{-9}$	$6.49 \cdot 10^{-9}$
20 km	$4.57 \cdot 10^{-9}$	$4.77 \cdot 10^{-9}$
30 km	$2.92 \cdot 10^{-9}$	$3.06 \cdot 10^{-9}$
60 km	$1.21 \cdot 10^{-9}$	$1.25 \cdot 10^{-9}$

15 Demonstrators

Demonstrator parameters are to be reviewed pending the October 2024 demonstrator workshop.

15.1 Cooling Cell Demonstrator

A cooling cell is composed of two or more solenoids (coils), an RF Structure made of one or multiple RF cells, and one or two absorbers made of low-Z materials.

The Collaboration adopts the terminology in Fig. 15.1 to designate the elements of a cooling cell.

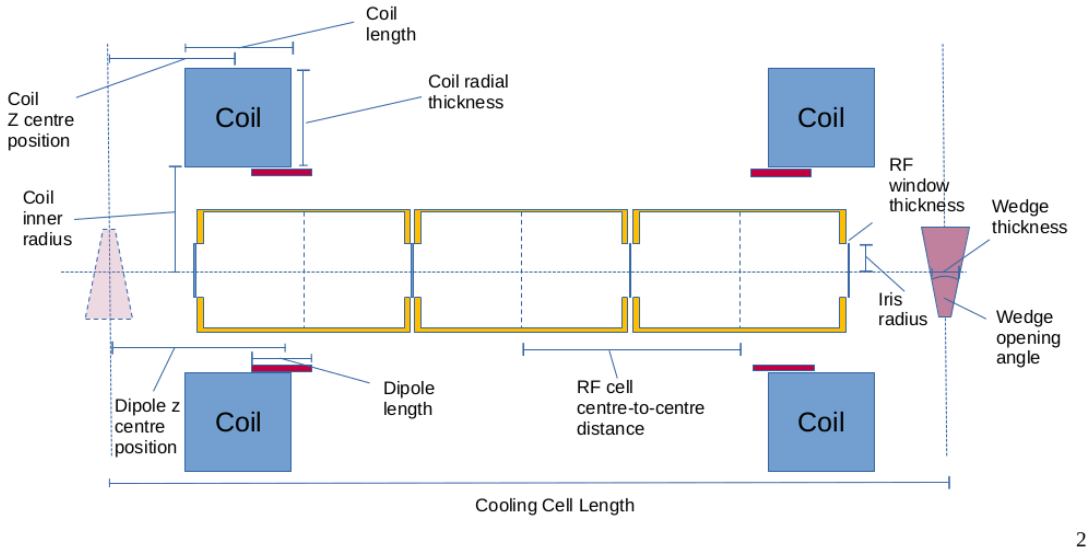

Fig. 15.1: Cooling Cell Schematic

The cooling cells efficiency impacts the performances of the entire complex, since it determines the intensity of the two beams and their emittance at the entrance of the acceleration sections. This means that an efficient design relaxes the requirements of all the downstream chain, and therefore both the overall cost and the feasibility. For this reason designing and testing a real scale cooling cell has the highest priority for the IMCC collaboration. The cooling section comprises of several different types of cooling cells therefore the choice of which one to build first to feel confident about the feasibility of the entire chain has been discussed at several occasions and is the object of a workpackage of the MuCol EU funded project. In this framework a workshop was organised in January 2024, leading to choices that have been reconfirmed during the annual meeting of the IMCC and MuCol, and that are listed in Tab. 15.1. The rationale behind those choices is to have a cell with challenging perfomances, but still within reach with a reasonable investment and in reasonable (5 to 7 years) time. Such a long delay is justified by the fact that we will use a new technology for the coils of the solenoid, based on REBCO HTS tapes, for which a few solenoids have been built but none is operated in a regular basis. We decided therefore not to target the maximum field of 20 T, but an intermediate 7 T, which is still very challenging for this technology but considered within reach. Studies for more challenging solenoids will progress in parallel independently from the cooling cell. For RF, there are two main difficulties,

reaching high average fields (40 MV/m) in a high magnetic field, that enhances breakdown phenomena. Mitigation measures are therefore studied and will be applied for a long term study in the cooling cell demonstrator, after dedicated studies in an RF test stand with magnetic field. Finally, the LiH (Lithium Hydride) technology has been chosen to start with because of the absence of major safety risks, but we plan to make sure that LH2 (Liquid Hydrogen) and GH2 (Gaseous Hydrogen) absorbers may be tested once all the technical and safety issues will be understood in a separate R&D programme. MuCol will fund the design of the cell while its construction has still to be funded. The programme proposes to test the cell in a dedicated test stand at full power, and then test its features with a beam in the Ionisation Cooling demonstrator facility described in the next paragraph.

15.2 TT7 Demonstrator

Once the cooling cell integration and dedicated tests are concluded, it is proposed that the performance and efficiency of a cooling channel composed of series of cooling cells are characterised in a beam test. Two potential sites have been identified on the CERN premises that can host the demonstrator facility. Here we focus on the TT7 tunnel option, which would be suitable only for a low-power target (10 kW) due to radiation protection restrictions but would reuse existing infrastructure. Fig. 15.2 shows engineering drawings of the TT7 tunnel, while a non-site specific conceptual layout of the demonstrator facility is shown in Fig. 15.3. Parameters pertaining to various facility subsystems that have been produced in preliminary design studies or have been assumed (e.g. proton beam) are listed in Tab. 15.2. The ongoing beam physics design of the target and pion/muon transport line sections rests on the assumption that the target would be housed in the cavern in the middle region of the TT7 tunnel.

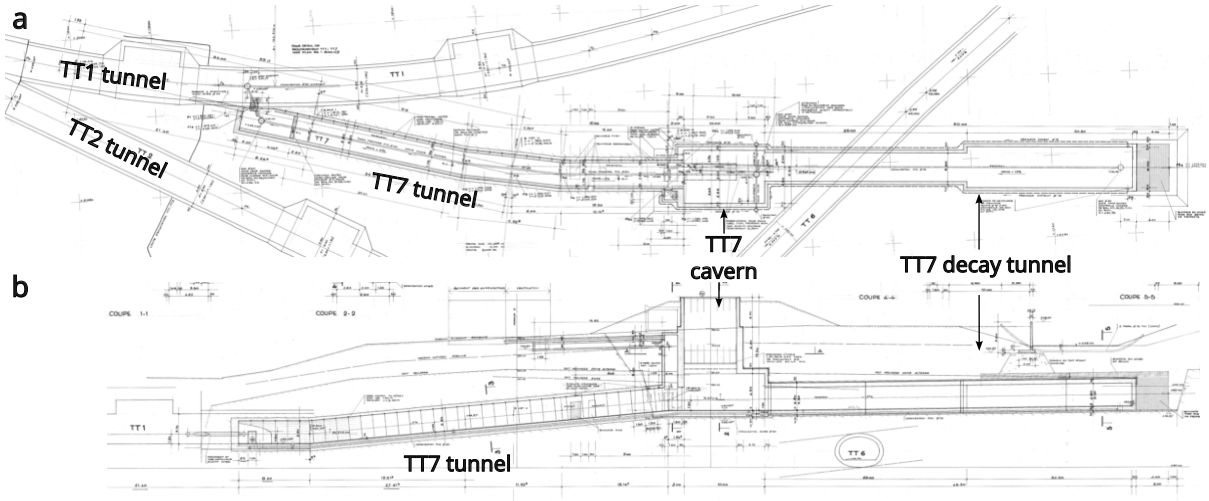

Fig. 15.2: a) Top and b) side view of the TT7 tunnel.

Protons would be provided by the CERN Proton Synchrotron (PS) and extracted via the TT2 tunnel through part of the TT1 tunnel into the TT7 tunnel. The proton beam would then be directed towards a 80–100 cm-long graphite target situated inside a magnetic horn designed to focus the secondary pions with a central momentum of $300\,\mathrm{MeV/c}$. A nTOF-like proton beam is currently assumed, albeit with the beam energy reduced to $14\,\mathrm{GeV}$ due to the beam power restrictions. Dedicated PS machine development studies are required to optimize the beam characteristics at this energy, in particular the bunch intensity and length. A magnetic horn was chosen over a solenoid-based pion capture solution due to its relatively

Parameter	Unit	Value	
Cooling Cell Length	mm	800	
Beam Physics			
Momentum	MeV/c	200	
Twiss beta function	mm	107	
Dispersion in X	mm	38.5	
Dispersion in Y	mm	20.3	
Beam Pipe Radius	mm	81.6	
Solenoid Parameters			
	Unit	Value	Tol
B0	T	8.75	0.25
B0.5	T	0	0.02
B1	T	1.25	0.025
B2	T	0	0.5
Coil Geometry			
Inner Radius	mm	250	
Length	mm	140	
Radial Thickness	mm	169.3	
Z Centre Position	mm	100.7	
Current Density	A/mm^2	500	
RF Cavity			
Center-to-centre distance	mm	188.6	
Gradient E0	MV/m	30	
Iris Radius	mm	81.6	
Number of RF Cells		3	
Frequency	GHz	0.704	
Synchronous Phase	degree	20	
Window Thickness	mm	0.1	
Wedge			
Material		LiH	
Opening Angle	degree	10	
Thickness	mm	20	
Alignment		Horizontal	
Dipole			
Length	mm	100	
Polarity		+ - - +	
Field	T	0.2	
Z Centre Position	mm	160	
Field Direction		Vertical	

Table 15.1: Cooling Cell Table

compact build given the available space within the existing cavern, and due to cost-effectiveness. The target and horn parameters shown here are the outcome of a first-pass optimisation study, with further design work required [57].

The design of the transport line downstream of the target is ongoing. It is forseen that a 8–10 m quadrupole-based lattice will be used as a pion decay channel, followed by a chicane used for muon momentum selection and for allowing the unspent protons and secondary particles to be dumped. A preliminary beam physics design for a beam preparation system, which would be used to tune the trans-

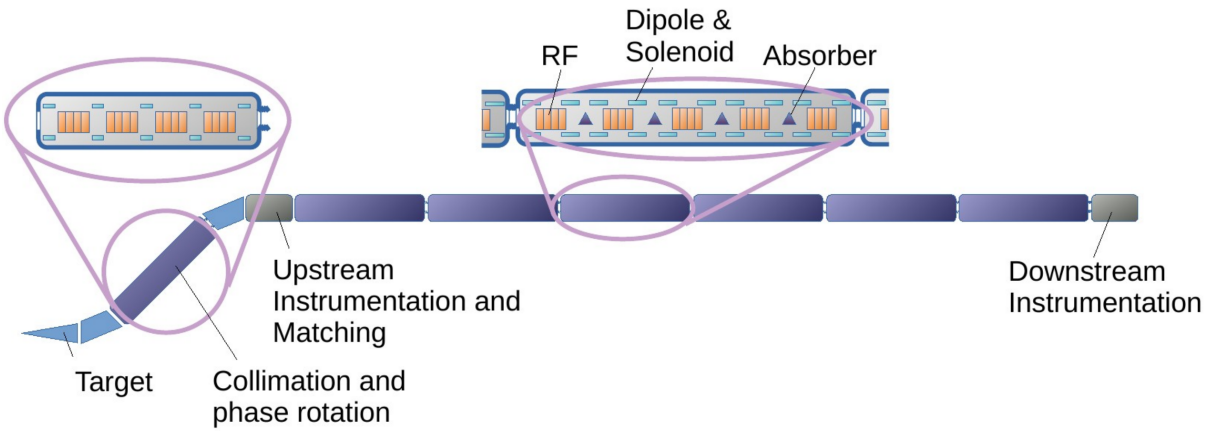

Fig. 15.3: Cooling demonstrator conceptual layout.

verse emittance and length of the muon bunches prior to their delivery to the cooling section, has been established [58]. Due to the limited available space in the TT7, it is expected that this system will be integrated within the chicane and may undergo further alterations.

The TT7 cooling channel would be composed of a series of 40 cooling cells grouped into vacuum vessels, as shown in Fig 15.3. The cooling performance for two different cooling channel lengths is listed in Tab. 15.3.

Parameter	Unit	Baseline value	Aspirational value
Transfer tunnel		TT7	–
Tunnel ramp	degrees	5.18	–
Pion decay channel length	m	8-10	20
Chicane length	m	12.8	–
Muon bunch intensity	10^6	1-10	100
Proton Beam			
Accelerator		Proton Synchrotron	SPS
Cycle		nTOF-like	–
Energy	GeV	14	26, 100
1-sigma beam size	mm	2	<2
1-sigma bunch length	ns	10	<10
Bunch intensity	10^{13}	1	>1
Target System			
Target material		Graphite	–
Target length	cm	80-100	–
Target radius	mm	6	–
Pion capture		Magnetic horn	Solenoid
Horn length	m	2	–
Horn current	kA	220	–
Beam Preparation System			
Cell length	m	1	–
Peak solenoid field on-axis	T	0.5	–
Collimator radius	m	0.05	–
Dipole field	T	0.67	–
Dipole length	m	1.04	–
RF real estate gradient	MV/m	7.5	–
RF nominal phase	degrees	0	–
RF frequency	MHz	704	–
Cooling channel			
Length	m	32	48
Number of cooling cells		40	60
Number of vacuum vessel modules		8	12
Number of cooling cells per vacuum vessel		5	5

Table 15.2: Demonstrator design based off CERN PS TT7 geometry

Simulated cooling performance	Unit	Start value	End value (32 m)	End value (48 m)
Transverse emittance	mm	2.37	1.61	1.44
Longitudinal emittance	mm	4.99	3.89	3.58
6D emittance	mm^3	26.21	9.77	7.12

Table 15.3: Simulated cooling performance.

16 Site-Based Designs Considerations

Tenative parameter tables to guide future design efforts for the existing site options. Different assumptions were made for the initial beam parameters and magnet technologies.

16.1 RCS Layout at CERN

The RCS layout on the CERN site is based on the usage of the existing Super Proton Synchrotron (SPS) and Large Hadron Collider (LHC) tunnels to host the high-energy acceleration chain. To make a comparison with the greenfield study possible, the same assumptions for the injection energy and the injection bunch population were chosen. The survival rate over the whole RCS chain is assumed as 70%, only considering losses due to muon decay, while the individual survival rates of the rings were adjusted to achieve a high extraction energy from the last RCS. Table 16.1 and 16.2 for the site-based design correspond to Table 7.1 and 7.2 for the greenfield design respectively.

Parameter	Unit	RCS SPS	RCS LHC1	RCS LHC2
Hybrid RCS	-	No	No	Yes
Repetition rate	Hz	5	5	5
Circumference	m	6912	26659	26659
Injection energy	GeV	63	350	1600
Extraction energy	GeV	350	1600	3800
Energy ratio	-	5.6	4.6	2.4
Assumed survival rate	-	0.88	0.86	0.92
Total survival rate	-	0.88	0.76	0.70
Acceleration time	ms	0.45	2.60	4.42
Revolution period	µs	23.0	88.9	88.9
Number of turns	-	19	29	50
Required energy gain per turn	GeV	15.1	43.1	44.4
Average acel. gradient	MV/m	2.15	1.62	1.68
Number of bunches	-	1	1	1
Inj bunch population	10^{12}	2.70	2.38	2.04
Ext bunch population	10^{12}	2.38	2.04	1.88
Beam current per bunch	mA	18.75	4.29	3.68
Beam power	MW	803	523	462
Vert. norm. emittance	µm	25	25	25
Hor. norm. emittance	µm	25	25	25
Long. norm emittance	eVs	0.025	0.025	0.025
Bunch length	ps	33.2	19.3	11.1
Straight section length	m	2809	8000	8000
Length with NC magnets	m	4103	18650	12940
Length with SC magnets	m	-	-	5680
Max NC dipole field	T	1.8	1.8	1.8
Max SC dipole field	T	-	-	10
Ramp rate	T/s	3320	1400	810
Main RF frequency	GHz	1.3	1.3	1.3

Table 16.1: Key acceleration Parameters for the CERN-site based RCS Acceleration Chain

Parameter	Unit	RCS SPS	RCS LHC1	RCS LHC2
Harmonic number		29900	115345	115345
Packing Fraction	%	0.59	0.70	0.70
Transition Gamma	-	33	45	58
Momentum compaction factor	10^{-4}	9	5	3

Table 16.2: Additional Parameters for the CERN-based RCS Acceleration Chain

16.1.1 RF system for the RCS layout at CERN

The design of the RF system for the RCS is based on the same assumptions as the RF system for the greenfield study. The assumptions are presented in 12.3.

		RCS SPS	RCS LHC1	RCS LHC2	All
Synchronous phase	°	135	135	135	-
Number of bunches/species	-	1	1	1	-
Combined beam current (μ^+, μ^-)	mA	37.5	8.58	7.35	-
Total RF voltage	GV	21.4	61	62.8	145.2
Total number of cavities	-	686	1958	2017	4661
Total number of cryomodules	-	77	218	225	520
Total RF section length	m	974	2760	2850	6584
Combined peak beam power (μ^+, μ^-)	MW	803	523	462	-
External Q-factor	10^6	0.79	3.49	4.07	-
Cavity detuning for beam loading comp.	kHz	-1.16	-0.26	-0.23	-
Beam acceleration time	ms	0.45	2.6	4.42	-
Cavity filling time	ms	0.194	0.854	0.993	-
RF pulse length	ms	0.644	3.454	5.413	-
RF duty factor	%	0.32	1.73	2.71	-
Peak cavity power	kW	987	228	195	-
Total peak RF power	MW	905	569	529	-
Total number of klystrons	-	99	60	54	213
Cavities per klystron	-	7	33	38	-
Average RF power	MW	2.91	10.3	14.3	27.51
Average wall plug power for RF System	MW	4.48	15.8	22	42.28
HOM power losses per cavity per bunch	kW	13.08	4.54	5.15	-
Average HOM power per cavity	W	58	118	227	-

Table 16.3: RF Parameters for the CERN-based RCS Acceleration Chain. For the synchronous phase, 90° is defined as being on-crest

16.2 RCS Layout at FNAL

Parameter	Unit	RCS1	RCS2	RCS3	RCS4
Hybrid RCS	-	No	Yes	Yes	Yes
Repetition rate	Hz	5	5	5	5
Circumference	m	6280	10500	15500	15500
Injection energy	GeV	173	450	1725	3035
Extraction energy	GeV	450	1725	3035	4059
Energy ratio	-	2.6	3.83	1.759	1.338
Assumed survival rate	-	0.85	0.83	0.946	0.972
Total survival rate	-	0.85	0.71	0.67	0.65
Acceleration time	ms	0.97	3.71	3.22	2.44
Revolution period	μs	21	35	51.7	51.7
Number of turns	-	46	106	62	47
Required energy gain per turn	GeV	6	12	21	21.7
Average acel. gradient	MV/m	0.96	1.15	1.64	1.62
Number of bunches	-	1	1	1	1
Inj bunch population	10^{12}	3.3	2.83	2.35	2.22
Ext bunch population	10^{12}	2.83	2.35	2.22	2.16
Vert. norm. emittance	mm	0.025	0.025	0.025	0.025
Hor. norm. emittance	mm	0.025	0.025	0.025	0.025
Long. norm emittance	eVs	0.025	0.025	0.025	0.025
Straight section length	m	1068	1155	1107	1107
Length with NC magnets	m	5233	7448	8495	6644
Length with SC magnets	m	-	1897	1930	2876
Max NC dipole field	T	1.8	1.8	1.75	1.75
Max SC dipole field	T	-	12	14	14
Ramp rate	T/s	1134	970	1087	1434
Main RF frequency	GHz	1.3	1.3	1.3	1.3

Table 16.4: Key Parameters for the Fermilab-based RCS Acceleration Chain

Bibliography

[1] IMCC & MuCol authors. “Milestone Report No. 3: Tentative Parameters Available”. In: *MuCol - A Design Study for a Muon Collider complex at 10 TeV centre of mass* (2023).

[2] M.A. Palmer and the MAP collaboration. “The US Muon Accelerator Program”. In: *arXiv* (2015). Available at doi:10.48550/arXiv.1502.03454. arXiv: 1502.03454 [physics.acc-ph].

[3] M. Aiba. *Accumulator Lattice Design For SPL Beam*. Tech. rep. CERN-NUFACT-Note-151. Geneva, Switzerland: CERN, Feb. 2007.

[4] E. Benedetto. *Beam stability in the SPL-Proton Driver accumulator for a Neutrino Factory at CERN*. Tech. rep. CERN-NUFACT-Note-156. Available at doi:10.1063/1.3399319. Geneva, Switzerland: CERN, Nov. 2009.

[5] M. Aiba. *Compressor Lattice Design for SPL Beam*. Tech. rep. CERN-NUFACT-Note-153. Geneva, Switzerland: CERN, Oct. 2007.

[6] E. Sargsyan. “LINAC4 H- source studies and future developments”. In: *IMCC Annual Meeting*. Available at link. France, 2023.

[7] S. Johannesson et al. “Initial design of a proton complex for the Muon Collider”. In: *Proc. IPAC’24*. Available at doi:10.18429/JACoW-IPAC2024-WEPR24. Nashville, TN, May 2024, pp. 2528–2531.

[8] C. T. Rogers et al. “Muon front end for the neutrino factory”. In: *Phys. Rev. ST Accel. Beams* 16 (2013), p. 040104. DOI: 10.1103/PhysRevSTAB.16.040104.

[9] Diktys Stratakis et al. “Design and Optimization of a Particle Selection System for Muon based Accelerators”. In: *5th International Particle Accelerator Conference*. June 2014, TUPME022. DOI: 10.18429/JACoW-IPAC2014-TUPME022.

[10] C. Yoshikawa et al. “A Charge Separation Study to Enable the Design of a Complete Muon Cooling Channel”. In: *1st North American Particle Accelerator Conference*. Sept. 2013.

[11] Yu Bao et al. “Conceptual design and modeling of a six-dimensional bunch merging scheme for a muon collider”. In: *Phys. Rev. Accel. Beams* 19.3 (2016), p. 031001. DOI: 10.1103/PhysRevAccelBeams.19.031001.

[12] Ruihu Zhu et al. “Performance and tolerance study of the rectilinear cooling channel for a muon collider”. In: (Sept. 2024). arXiv: 2409.02613 [physics.acc-ph].

[13] F. Batsch et al. “Longitudinal beam dynamics and RF requirements for a chain of muon RCSs”. In: *Proc. IPAC’23* (Venice, Italy). JACoW Publishing, Geneva, Switzerland, May 2023, pp. 1428–1431. DOI: 10.18429/JACoW-IPAC2023-TUPA040. URL: https://jacow.org/ipac2023/doi/jacow-ipac2023-tupa040.

[14] J. S. Berg. “Details and justifications for the MAP concept specification for acceleration above 63 GeV”. In: BNL-105415-2014-IR (Feb. 2014). DOI: doi:10.2172/1149436. URL: https://www.bnl.gov/isd/documents/86226.pdf.

[15] J. S. Berg. “Muon Collider Pulsed Synchrotron Parameters”. In: BNL-221336-2021-INRE (Apr. 2021). DOI: 10.2172/1779395. URL: https://www.osti.gov/biblio/1779395.

[16] N. V. Mokhov et al. “Muon Collider Interaction Region and Machine-detector Interface Design”. In: *Proc. PAC'11*. New York, NY, USA, Mar. 2011, pp. 82–84.

[17] N. V. Mokhov and S. I. Striganov. “Detector backgrounds at Muon Colliders”. In: *Physics Procedia* 37 (2012). Available at doi:10.1016/j.phpro.2012.03.761, pp. 2015–2022.

[18] D. Calzolari and K. Skoufaris. “Machine-detector interface studies for a multi-TeV muon collider”. In: *PoS* ICHEP2022 (2022). Available at doi:10.22323/1.414.0063, p. 063.

[19] D. Calzolari et al. “Lattice and detector studies for the MDI of a 10 TeV muon collider”. In: *Proc. IPAC'23*. Available at doi:10.18429/JACoW-IPAC2023-MOPA090. Venice, Italy, May 2023, pp. 252–255.

[20] MA Palmer. “The US muon accelerator program”. In: *arXiv preprint arXiv:1502.03454* (2015).

[21] Zachary S. Hartwig et al. “The SPARC Toroidal Field Model Coil Program”. In: *IEEE Transactions on Applied Superconductivity* 34.2 (2024), pp. 1–16. DOI: 10.1109/TASC.2023.3332613.

[22] *MIT Press release*. URL: https://news.mit.edu/2021/MIT-CFS-major-advance-toward-fusion-energy-0908.

[23] L. Bottura et al. “Design and analysis of a HTS internally cooled cable for the Muon Collider target magnet”. In: submitted for publication to Cryogenics, 2023.

[24] C. Accettura et al. “Conceptual Design of a Target and Capture Channel for a Muon Collider”. In: vol. 34. 5. 2024, pp. 1–5. DOI: 10.1109/TASC.2024.3368387.

[25] Diktys Stratakis and Robert B Palmer. “Rectilinear six-dimensional ionization cooling channel for a muon collider: A theoretical and numerical study”. In: *Physical Review Special Topics-Accelerators and Beams* 18.3 (2015), p. 031003.

[26] Robert B Palmer, Richard C Fernow, and Jon Lederman. *Muon Collider Final Cooling in 30-50 T Solenoids*. Tech. rep. Brookhaven National Lab.(BNL), Upton, NY (United States), 2011.

[27] Ruihu Zhu et al. “Performance and tolerance study of the rectilinear cooling channel for a muon collider”. In: *arXiv preprint arXiv:2409.02613* (2024).

[28] *FujiKura ReBCO HTS*. URL: https://www.fujikura.co.jp/eng/products/newbusiness/superconductors/01/superconductor.pdf.

[29] Shinji Fujita et al. “Flux-pinning properties of BaHfO 3-doped EuBCO-coated conductors fabricated by hot-wall PLD”. In: *IEEE Transactions on Applied Superconductivity* 29.5 (2019), pp. 1–5.

[30] B. Bordini et al. “Conceptual Design of a ReBCO Non/Metal-Insulated Ultra-High Field Solenoid for the Muon Collider”. In: *IEEE Transactions on Applied Superconductivity* 34.3 (2024), pp. 1–10. DOI: 10.1109/TASC.2024.3361881.

[31] J Scott Berg and Holger Witte. “Pulsed synchrotrons for very rapid acceleration”. In: *AIP Conference Proceedings*. Vol. 1777. 1. AIP Publishing. 2016.

[32] M. Breschi et al. “Comparative Analysis of Resistive Dipole Accelerator Magnets for a Muon Collider”. In: *IEEE Transactions on Applied Superconductivity* 34.5 (2024), pp. 1–5. DOI: 10.1109/TASC.2024.3360208.

[33] Daniel Novelli et al. “Analytical Evaluation of Dipole Performance Limits for a Muon Collider”. In: *IEEE Transactions on Applied Superconductivity* 34.5 (2024), pp. 1–5. DOI: 10.1109/TASC.2024.3352526.

[34] Daniel Novelli et al. “Analytical and numerical study of superconducting dipole and quadrupole performance limits for a Muon Collider”. In: *The Applied Superconductivity Conference (ASC 2024)*. Vol. 3LPO2H-05. 2024.

[35] Carmelo Barbagallo and Alexej Grudiev. “Conceptual RF design and modelling of a 704 MHz cavity for the muon cooling complex”. In: *JACoW* IPAC2024 (2024), WEPR25. DOI: 10.18429/JACoW-IPAC2024-WEPR25.

[36] C. Arnaud et al. “Status Report on Superconducting NB Cavities for LEP”. In: (1989). Available at https://accelconf.web.cern.ch/SRF89/papers/srf89a02.pdf.

[37] C. Adolphsen et al. “The International Linear Collider Technical Design Report - Volume 3.II: Accelerator Baseline Design”. In: *arXiv* (2013). Available at doi.org:10.48550/arXiv.1306.6328.

[38] E. Plawski. “The Wakefields and Loss Factors in Superconducting Accelerating Cavities for TESLA Collider”. In: *Proceedings of the Particle Accelerator Conference*. Available at doi.org:10.1109/PAC.1999.792319. 1999.

[39] D. Proch. “The TESLA Cavity: Design Considerations and RF Properties”. In: *Proceedings of the Sixth Workshop on RF Superconductivity*. Available at https://accelconf.web.cern.ch/SRF93/papers/srf93g01.pdf. Newport News, United States, 1993, pp. 382–397.

[40] B. Aune et al. “Superconducting TESLA cavities”. In: *Phys. Rev. ST Accel. Beams* 3 (9 Sept. 2000), p. 092001. DOI: 10.1103/PhysRevSTAB.3.092001. URL: https://link.aps.org/doi/10.1103/PhysRevSTAB.3.092001.

[41] J. Sekutowicz et al. “Design of a Low Loss SRF Cavity for the ILC”. In: *Proceedings of PAC 2005*. Available at https://accelconf.web.cern.ch/p05/papers/tppt056.pdf. Knoxville, United States, 2005.

[42] D. Amorim. *Single bunch transverse instabilities in the RCS with TESLA or Low Loss SRF cavities*. Available at https://indico.cern.ch/event/1408565/contributions/5988720.

[43] E. Kvikne. *Eddy currents*. Available at https://indico.cern.ch/event/1325963/contributions/5806753/.

[44] D. Amorim. *Report about the follow-up meeting on "RCS normal conducting magnets vacuum chamber*. Available at https://indico.cern.ch/event/1408565/contributions/5988712.

[45] *Xsuite*. Available at https://github.com/xsuite. Accessed 2024.

[46] *PyHEADTAIL*. Available at https://github.com/PyCOMPLETE/PyHEADTAIL. Accessed 2024.

[47] D. Amorim. *Collective effects and start-to-end simulations*. Available at https://indico.cern.ch/event/1325963/contributions/5806745/.

[48] A. Lechner. “Shielding Requirements for the Collider Ring Magnets”. In: *IMCC Annual Meeting 2023*. Available at https://indico.cern.ch/event/1250075/contributions/5342853/. Orsay, France, 2023.

[49] K.-Y. Ng. *The Quasi-Isochronous Buckets of the Muon Collider*. Tech. rep. FN-648. Available at https://lss.fnal.gov/archive/test-fn/0000/fermilab-fn-0648.pdf. Batavia, Illinois: Fermilab, 1995.

[50] E. S. Kim and M. Yoon. "Transverse beam instability in a 50-GeV x 50-GeV muon-collider ring". In: *Nucl. Instrum. Meth. A* 470 (2001), pp. 473–481. DOI: 10.1016/S0168-9002(01)00793-8.

[51] D. Amorim. *Update on Impedances and Instabilities*. Available at https://indico.cern.ch/event/1325963/contributions/5837721/.

[52] N. V. Mokhov et al. "Radiation Effects in a Muon Collider Ring and Dipole Magnet Protection". In: *Proc. PAC'11*. New York, NY, USA, Mar. 2011, pp. 2294–2296.

[53] V. Kashikhin et al. "High-Field Combined-Function Magnets for a 1.5 TeV Muon Collider Storage Ring". In: *Proc. IPAC'12*. New Orleans, LA, USA, May 2012, pp. 3587–3589.

[54] N. V. Mokhov et al. "Mitigating Radiation Impact on Superconducting Magnets of the Higgs Factory Muon Collider". In: *Proc. IPAC'14*. Available at doi:10.18429/JACoW-IPAC2014-TUPRO030. Dresden, Germany, June 2014, pp. 1084–1086.

[55] D. Calzolari et al. "Radiation Load Studies for Superconducting Dipole Magnets in a 10 TeV Muon Collider". In: *Proc. IPAC'22*. Available at doi:10.18429/JACoW-IPAC2022-WEPOST001. Bangkok, Thailand, June 2022, pp. 1671–1674.

[56] A. Lechner et al. "Radiation shielding studies for superconducting magnets in multi-TeV muon colliders". In: *Proc. IPAC'24* (Nashville, TN). Available at doi:10.18429/JACoW-IPAC2024-WEPR26. May 2024, pp. 2536–2539.

[57] P. B. Jurj. *Cooling Demonstrator Design Update*. Available at https://indico.cern.ch/event/1325963/contributions/5793112/.

[58] Chris Rogers. "A Demonstrator for Muon Ionisation Cooling". In: *Physical Sciences Forum* 8.1 (2023). ISSN: 2673-9984. DOI: 10.3390/psf2023008037. URL: https://www.mdpi.com/2673-9984/8/1/37.